Phosphorylation of phase-separated p62 bodies by ULK1 activates a redox-independent stress response

Ryo Ikeda[1,2], Daisuke Noshiro[3], Hideaki Morishita[1], Shuhei Takada[1], Shun Kageyama[1],

5 **Yuko Fujioka[3], Tomoko Funakoshi[1], Satoko Komatsu-Hirota[1], Ritsuko Arai[4], Elena Ryzhii[4], Manabu Abe[5], Tomoaki Koga[6], Mitsuyoshi Nakao[6], Kenji Sakimura[5], Arata Horii[2], Satoshi Waguri[4], Yoshinobu Ichimura[1,*], Nobuo N Noda[3,*] and Masaaki Komatsu[1,*]**

10 [1]Department of Physiology, Juntendo University Graduate School of Medicine, Bunkyo-ku, Tokyo 113-8421, Japan

[2]Department of Otolaryngology Head and Neck Surgery, Niigata University Graduate School of Medical and Dental Sciences, Chuo-ku, Niigata 951-8510, Japan

[3]Institute for Genetic Medicine, Hokkaido University, Kita-Ku, Sapporo, 060-0815, Japan

15 [4]Department of Anatomy and Histology, Fukushima Medical University School of Medicine, Hikarigaoka, Fukushima 960-1295, Japan

[5]Department of Animal Model Development, Brain Research Institute, Niigata University, Chuo-ku, Niigata 951-8510, Japan

[6]Department of Medical Cell Biology, Institute of Molecular Embryology and Genetics,

20 Kumamoto University, Chuo-ku, Kumamoto 860-0811, Japan

*Correspondence should be addressed to Yoshinobu Ichimura, Nobuo N Noda or Masaaki Komatsu (e-mail: yichimu@juntendo.ac.jp, nn@igm.hokudai.ac.jp, mkomatsu@juntendo.ac.jp).

25

Running title: Stress response by phase-separated p62

Abstract

NRF2 is a transcription factor responsible for antioxidant stress responses that is
30 **usually regulated in a redox-dependent manner. p62 bodies formed by liquid-liquid phase separation contain Ser349-phosphorylated p62, which participates in the redox-independent activation of NRF2. However, the regulatory mechanism and physiological significance of phosphorylation remain unclear. Herein, we identify ULK1 as a kinase responsible for phosphorylation of p62. ULK1 co-localizes with p62 bodies, and directly**
35 **interacts with p62. This phosphorylation allows KEAP1 to be retained within p62 bodies, activating NRF2. $p62^{S351E/+}$ mice are phosphomimetic knock-in mice in which Ser351 corresponding to human Ser349 is replaced by Glu. These mice, but not phosphodefective $p62^{S351A/S351A}$ mice, exhibit NRF2 hyperactivation and growth retardation, the latter caused by malnutrition and dehydration due to obstruction of**
40 **the esophagus and forestomach secondary to hyperkeratosis. $p62^{S351E/+}$ mice are a phenocopy of systemic *Keap1*-knockout mice. Our results expand our understanding of the physiological importance of the redox-independent NRF2 activation pathway and provide new insight into the role of phase separation in this process.**

Introduction

Liquid-liquid phase-separated biomolecular condensates, liquid droplets play an important role in many biological processes, such as gene expression, protein translation, stress response, and protein degradation, by incorporating a variety of RNA and client proteins into their interior depending on the intracellular context [1]. Autophagy is involved in the degradation of several cytoplasmic liquid droplets, including stress granules and P bodies, and defects in this process are thought to cause transition of these droplets to the solid phase, resulting in the development of intractable diseases such as neurodegenerative disorders and cancer [2,3]. Of the droplets that have a unique biological function and are degraded by autophagy, p62 bodies (also called p62 droplets) are liquid droplets formed by liquid-liquid phase separation (LLPS) of p62 and its binding partners, ubiquitinated proteins [4,5]. p62 bodies are involved in the regulation of intracellular proteostasis through their own autophagic degradation, and also contribute to the regulation of the major stress-response mechanism by sequestration of a client protein, kelch-like ECH-associated protein 1 (KEAP1) [6,7].

An Unc-51-like kinase 1 (ULK1) phosphorylates p62 at Ser407, inhibiting dimer formation of the UBA domain of p62 [8,9], and subsequent phosphorylation of Ser403 by TBK1, CK2, TAK1, and ULK1 allows binding of ubiquitinated proteins [8,10-12]. These phosphorylation events are thought to promote LLPS [4,5]. In the degradation of p62 bodies, the ULK1 protein kinase complex consisting of FIP200/RB1-inducible coiled-coil protein 1 (hereafter as FIP200), ULK1, ATG13, and ATG101 is translocated onto the bodies by binding of the FIP200 Claw domain to p62 [13]. Alternatively, the ULK1 protein kinase complex is recruited to p62 bodies through the interaction of FIP200 with TAX1BP1, which localizes at p62 bodies through the interaction with a p62 binding partner NBR1 [14]. Subsequently, ATG proteins assemble around the bodies [15]. In the end, the p62 bodies are surrounded by autophagosomes due to the wetting effect [16] and the binding of LC3 or GABARAP to p62 on the isolation membrane [15], followed by lysosomal degradation.

KEAP1 is an adaptor protein of cullin 3 ubiquitin ligase for nuclear factor (erythroid-derived 2)-like 2 (NRF2), which is a key transcription factor for a series of genes encoding anti-oxidative proteins and enzymes [17]. In the canonical pathway, KEAP1 is inactivated by the modification of oxidants, and NRF2 is then activated via redox-dependent regulation [17]. This redox-dependent pathway has been shown to be important in redox, metabolism, and protein homeostasis, as well as in the regulation of inflammation and cellular protection against many pathological conditions [17,18]. In addition to this canonical pathway, a specific region of p62 directly interacts with KEAP1, competitively preventing the interaction

between KEAP1 and NRF2 [19]. The phosphorylation of Ser349 locating at the KEAP1-interacting region of p62 enhances the interaction of p62 with KEAP1, sufficiently resulting in full activation of NRF2 independently of redox conditions [20]. However, the kinase(s) and

85   regulatory mechanism underlying the redox-independent pathway, as well as its physiological significance, remain unclear.

    Herein, we show for the first time that ULK1 is a major kinase for Ser349 of p62, both *in vitro* and *in vivo*. ULK1 directly interacts with p62 and phosphorylates Ser349 of p62. ULK1 localizes in p62 bodies *in vitro* and *in vivo* in a FIP200-independent fashion. While

90   this phosphorylation does not affect the influx of KEAP1 into p62 bodies, it inhibits KEAP1 outflow, keeping KEAP1 in the p62 bodies and activating NRF2. Knock-in mice with a phosphomimetic mutation, but not those with a phosphodefective mutation, exhibit persistent activation of NRF2, which causes hyperkeratosis and consequently obstruction of the esophagus and forestomach, and eventually severe growth retardation due to malnutrition.

95   Taken together, these results indicate the physiological importance of p62 body- and ULK1-dependent and redox-independent stress response.

Results

ULK1 directly interacts with and phosphorylates p62

To clarify whether the UKL1 kinase itself has an effect on physical property and

100   physiological role of p62 bodies, we first studied physical interaction of p62 with ULK1 or

its yeast homologue Atg1 using high-speed atomic force microscopy (HS-AFM) (Fig. 1).

ULK1 has a serine-threonine kinase domain (KD) at the N-terminus and two microtubule

interaction and transport (MIT1 and 2) domains at the C-terminus, all of which are

conserved between yeast and mammals (Fig. 1a). The KD and MIT1/2 domains are linked

105   by an intrinsically disordered region (IDR) (Fig. 1b). p62 has an N-terminal Phox1 and

Bem1p (PB1) domain and C-terminal ubiquitin-associated (UBA) domain as well as several

interacting regions such as LIR and KIR located in an IDR between the PB1 and UBA

domains (Fig. 1a and b). We purified recombinant p62 (268–440 aa and 320–440 aa) and

SNAP-tagged ULK1 and Atg1 (Fig. 1c). HS-AFM of SNAP-ULK1 revealed that it contains

110   two globular domains consisting of a KD and two tandem MIT domains, which are linked to

each other with an IDR, like Atg1 [21] (Supplementary Fig. S1a and Supplementary Movie S1).

Meanwhile, HS-AFM of p62 (268–440 aa) visualized the homodimeric structure mediated

by the dimerization of the UBA domain, forming a hammer-shaped structure with IDRs

wrapped around each other (Supplementary Fig. S1b and Supplementary Movie S2). When

115   each SNAP-ULK1 and SNAP-Atg1 was mixed with p62 (268–440 aa), the p62 homodimer

directly bound to SNAP-ULK1 and SNAP-Atg1 via dynamic IDR-IDR and IDR-globular

domain interactions (Fig. 1d and e, Supplementary Fig. S1c, and Supplementary Movie S3

and 4). Consistent with this, ULK1 and Atg1 directly phosphorylated recombinant p62 (268–

440 aa and 320–440 aa) at Ser349 (Fig. 1f). Although Ser403 was hardly phosphorylated

120   (Fig. 1f), it was also phosphorylated when mCherry-tagged full-length p62 was used (Fig.

1f), indicating that the N-terminal PB1 domain of p62 is required for efficient Ser403

phosphorylation by ULK1 and Atg1. These data suggest that ULK1 directly interacts with

and phosphorylates p62.

125   **Localization of ULK1 in p62 bodies**

p62 undergoes LLPS upon interaction with ubiquitinated proteins *in vitro*, forming p62

condensates [4]. We examined whether SNAP-Atg1 and SNAP-ULK1 associate with p62

condensates *in vitro*. Consistent with previous reports [4,5,15], mixing mCherry-p62 with linear

octa-ubiquitin (8xUb) resulted in the formation of condensates (Fig. 2a). Their size was

130   increased by phosphomimetic p62 mutations (S403E and S407E) (Fig. 2a) that are known to

increase the binding affinity of p62 to ubiquitin [8,10,11]. SNAP-Atg1 and SNAP-ULK1 were

recruited to p62 condensates when all were incubated together (Fig. 2b), implying that both Atg1 and ULK1 associate with p62 even in the droplet form.

We next studied the localization of ULK1 in Huh-1 cells. Immunofluorescence
135   analysis with an anti-ULK1 antibody showed the significant signal of ULK1 in p62 bodies, which was diminished by ULK1 depletion (Fig. 2c, Supplementary Fig. S2). Together with FIP200, ATG13, and ATG101, ULK1 forms an initiation kinase complex for autophagosome formation [22], and p62 interacts with FIP200 through the Claw domain [13], raising the possibility that the localization of ULK1 to p62 bodies is indirect and depends on
140   the interaction of p62 with FIP200. To test this hypothesis, we developed *FIP200*-deficient Huh-1 cells (Supplementary Fig. S2). Remarkably, we observed ULK1 localization to p62 bodies even in these cells, and ULK1 signal intensity was significantly higher than in wild-type Huh-1 cells (Fig. 2c), probably due to increased ULK1 protein in the *FIP200*-knockout cells. Exogenously expressed green fluorescent protein (GFP)-tagged ULK1 and ULK2 also
145   localized on p62 bodies regardless of the presence of FIP200 (Fig. 2d). Correlative light and electron microscopy with Huh-1 cells harboring GFP-ULK1 revealed that GFP-ULK1 localizes on round structures composed of filamentous assemblies; these structures were previously identified as p62 bodies [15,23] (Fig. 2e). Taken together, these data suggest that ULK1 localizes in p62 bodies through the direct ULK1-p62 interaction.

150

Significance of ULK1 within p62 bodies

To investigate the significance of ULK1 and ULK2 within p62 bodies, we utilized MRT68921, which is the most potent inhibitor of ULK1 and ULK2, with IC_{50} values of 2.9 nM and 1.1 nM, respectively [24]. As predicted, the treatment of Huh-1 cells with MRT68921
155   decreased not only the level of phosphorylated ATG13, but also those of the Ser349- and Ser403-phosphorylated p62 forms (Fig. 3a and Supplementary Fig. S3). Similar results were obtained with ULK-101, another inhibitor of ULK1 and ULK2 [25] (Supplementary Fig. S4).

We observed extensive co-localization of the Ser403-phosphorylated form in p62 bodies (Fig. 3b). The signal intensity of Ser403-phosphorylated p62 in p62 bodies became
160   weaker when Huh-1 cells were treated with MRT68921 (Fig. 3b). MRT68921 treatment slightly but significantly decreased both the size and number of p62 bodies (Fig. 3b). These results suggest that while ULK1 and ULK2 contribute to the LLPS of p62 through the phosphorylation of Ser403 of p62, the dephosphorylation of Ser403 within p62 bodies hardly have an effect on already formed p62 bodies.

165   Next, we tested whether the inhibition of ULK1 and ULK2 affected KEAP1-localization within p62 bodies. Huh-1 cells were cultured in the presence or absence of

MRT68921 and immunostained with anti-p62 and anti-Ser349-phosphorylated p62-specific antibodies. The p62 bodies in Huh-1 cells contained the Ser349-phosphorylated form (Fig. 3c). Upon exposure to MRT68921, the signal intensities of phosphorylated p62 on p62

170 bodies markedly decreased (Fig. 3c). Double immunofluorescence analysis with anti-p62 and anti-KEAP1 antibodies showed extensive localization of KEAP1 in the p62 bodies (Fig. 3c). The signal intensity of KEAP1 in the bodies was significantly attenuated by treatment with MRT68921 (Fig. 3c), suggesting release of KEAP1 from the bodies to the cytoplasm and subsequent NRF2 inactivation. Indeed, gene expression of NRF2 targets such as

175 glutamate-cysteine ligase catalytic subunit (*GCLC*), NAD(P)H quinone dehydrogenase 1 (*NQO1*), UDP-glucose 6-dehydrogenase (*UGDH*), superoxide dismutase 1 (*SOD1*), and *p62* itself was decreased by MRT68921 treatment (Fig. 3d). These data suggest that ULK1 and ULK2 in p62 bodies contribute to the activation of NRF2 by phosphorylating p62 at Ser349 and promoting sequestration of KEAP1 within p62 bodies.

180

Dynamics of KEPA1 in S349-phosphorylated p62 bodies

In the next series of experiments, we sought to determine whether Ser349 phosphorylation of p62 affects KEAP1 dynamics in p62 bodies. To do this, we generated *p62 KEAP1* double-knockout Huh-1 cells (Supplementary Fig. S2) and expressed GFP-tagged wild-type p62,

185 phosphomimetic p62^{S349E} [20], phosphodefective p62^{S349A} [20], or KEAP1 interaction-defective p62^{T350A} [19] together with mCherry or mCherry-tagged KEAP1. The fluorescence analysis revealed that in the absence of mCherry-KEAP1, wild-type GFP-p62 and all GFP-p62 mutants formed round, liquid droplet-like structures (Fig. 4a). When we coexpressed wild-type GFP-p62 or the mutants with mCherry-KEAP1 in the double knockout Huh-1 cells,

190 mCherry-KEAP1 co-localized well with GFP-p62-positive structures except those composed of GFP-p62^{T350A} (Fig. 4a). We measured the circularity of each GFP-p62-positive structure composed of wild-type p62 or the mutants in the presence or absence of mCherry-KEAP1. Circularity values close to 1 were associated with liquid droplets, while lower values correlated with gels or aggregates [26,27]. In the absence of mCherry-KEAP1, all GFP-p62-

195 positive structure values were close to 1 (Fig. 4b), suggesting that they were liquid droplets. Remarkably, the circularity of GFP-p62^{S349E} bodies but not others was significantly decreased when these bodies co-localized with mCherry-KEAP1 (Fig. 4b). Further, *in vitro* LLPS assay revealed that introduction of the S349E mutation in p62$^{S403E\ S407E}$ resulted in the formation of amorphous aggregates rather than liquid droplets, but only in the presence of

200 KEAP1 (Fig. 4c and Supplementary Fig. S5). These data suggest that strong binding of

KEAP1 to p62 as a result of the S349E mutation changes the biophysical properties of p62 bodies.

We hypothesized that once mCherry-KEAP1 was incorporated into S349-phosphorylated p62 bodies, KEAP1 efflux from the bodies would be significantly reduced

205 due to the close interaction between the phosphorylated p62 and KEAP1. To prove this, we used fluorescence recovery after photobleaching (FRAP) and fluorescence loss in photobleaching (FLIP) [28] to evaluate KEAP1 influx and efflux into p62 bodies consisting of GFP-p62^{S349E} or p62^{S349A}. To measure the influx of mCherry-KEAP1 into GFP-p62 bodies, the whole fluorescence of mCherry-KEAP1 in GFP-p62^{S349E} or p62^{S349A} bodies was

210 photobleached, and the fluorescence recovery was measured. It is common to characterize molecular dynamics in FRAP experiments by the half-time of recovery (*t50*) and the mobile fraction [29]. Based on these parameters, the influx of mCherry-KEAP1 from the surrounding environment was comparable between p62^{S349E} and p62^{S349A} bodies (Fig. 4d and Supplementary Movies S5 and S6). Next, to examine the efflux of mCherry-KEAP1 from

215 GFP-p62 bodies, we carried out FLIP analysis. When approximately 80% of the cellular region is photobleached, the fluorescent signal in the cytoplasm is transiently reduced, followed by a gradual recovery due to influx from the non-bleached region. If there is an outflow of mCherry-KEAP1 from p62 bodies, the fluorescence intensity of mCherry-KEAP1 within p62 bodies in the non-bleached area should decrease after photobleaching. While the

220 signal intensity of mCherry-KEAP1 in p62^{S349A} bodies decreased about to $58.2 \pm 0.05\%$ of the baseline value at 30 min after the photobleaching, it remained higher ($72.0 \pm 0.07\%$) in the case of p62^{S349E} bodies (Fig. 4e and Supplementary Movies S7 and S8). Finally, to investigate the inner fluidity of mCherry-KEAP1 in GFP-p62 bodies, we measured the fluorescence recovery of mCherry-KEAP1 after photobleaching of the central portion of

225 GFP-p62 bodies. The *t50* of mCherry-KEAP1 in p62^{S349E} bodies was 8.51 ± 4.83 min, which was much slower than that seen with p62^{S349A} bodies (3.32 ± 1.23 min) (Fig. 4f and Supplementary Movie S9 and S10). Taken together, these results suggest that Ser349 phosphorylation of p62 results in the retention of KEAP1 in p62 bodies, and when this sequestration is prolonged, the inner fluidity of these bodies is decreased.

230

Physiological significance of Ser349 phosphorylation of p62 in mice

To clarify the physiological role of Ser349 phosphorylation of p62 *in vivo*, we generated knock-in mice that expressed p62 in which Ser351 (corresponding to human Ser349) was replaced by Glu (*p62$^{S351E/+}$* mice) or Ala (*p62$^{S351A/+}$* mice). Initially, we tried to use the

235 CRISPR/Cas9 system to generate both knock-in mice, but could obtain only *p62$^{S351A/+}$* mice.

We therefore attempted to use prime editing, a recently developed system, to generate $p62^{S351E/+}$ mice using mouse embryonic stem cells (mES cells) [30]. Even with this method, however, we were unable to obtain chimeric mice with high chimerism. We did succeed in generating a male chimeric mouse with low chimerism and germline transmission. *In vitro*

240 fertilization using sperm from the chimeric mouse was performed to obtain a sufficient number of heterozygotes for the experiments. The resulting $p62^{S351E/+}$ mice showed severe growth retardation and mild hepatomegaly at P12 and P15 (Fig. 5a-c), which is probably why knock-in mice could not be obtained by the above method. RNAseq analysis of wild-type and $p62^{S351E/+}$ mouse livers demonstrated increased gene expression of NRF2 targets

245 (Fig. 5d). Consistent with these results, real-time PCR analysis showed that the gene expression of NRF2 targets such as *glutathione S-transferase Mu 1* (*Gstm1*), *Nqo1*, *Ugdh*, and *p62* was much higher in the liver of $p62^{S351E/+}$ mice than in wild-type mice (Fig. 5e). We also found that the levels of GSTM1, NQO1, and UGDH, and the nuclear level of NRF2, were markedly higher in $p62^{S351E/+}$ mice than in wild-type mice (Fig. 5f). These results

250 indicate that the expression of $p62^{S351E}$ at half the level of endogenous $p62$ is sufficient for KEAP1 inactivation and subsequent NRF2 activation *in vivo*. Anatomical analysis revealed that the forestomach wall of $p62^{S351E/+}$ mice was obviously thickened compared with that of wild-type mice (Supplementary Fig. S6). Hematoxylin and eosin (HE) staining indicated that the esophagus and forestomach of $p62^{S351E/+}$ mice had a remarkably thicker stratum corneum

255 than those of wild-type mice, but such differences were not observed in the skin (Fig. 5g). In the forestomach, the epithelial layers below the stratum corneum were slightly thicker in $p62^{S351E/+}$ mice than in wild-type mice, but this was not evident in the esophagus. Immunohistochemistry (IHC) revealed that in the epithelia of the esophagus and forestomach, the intensity of NQO1 was higher in $p62^{S351E/+}$ mice than in wild-type mice

260 (Fig. 5h). The staining of the cell proliferation marker Ki-67 showed no significant difference between mutant and wild-type organs (data not shown). Serum data from $p62^{S351E/+}$ mice indicated a slightly but significantly elevated aspartate aminotransferase level, signs of malnutrition (low blood glucose and high cholesterol), and signs of dehydration (increased blood urea nitrogen and creatinine) (Fig. 5i). These results strongly

265 suggested that $p62^{S351E/+}$ mice are a phenocopy of *Keap1*-deficient mice [31], and that impaired nutritional intake due to hyperkeratosis in the esophagus and forestomach could be the primary cause of the severe phenotype of $p62^{S351E/+}$ mice. In striking contrast to these mice, $p62^{S351A/+}$ and $p62^{S351A/S351A}$ mice were fertile and showed no obvious growth retardation (Supplementary Fig. S7a-c). Morphological and biochemical analyses indicated no

270 differences in phenotypes (including NRF2 activation) between wild-type and $p62^{S351A/S351A}$

mice (Supplementary Fig. S7d-g), implying that Ser351 phosphorylation of p62 is unnecessary for mouse development and survival. Taken together, these results indicate that Ser351 phosphorylation of p62 is physiologically important for the control of NRF2 activity *in vivo*, most likely by regulating the redox-independent KEAP1-NRF2 pathway.

275

Discussion

The ULK1 kinase complex functions as the most upstream factor for autophagosome formation [22,32]. In *Saccharomyces cerevisiae*, nutrient deprivation causes phosphatase-induced dephosphorylation of Atg13, which results in the formation of higher-order

280 structures of the Atg1 kinase complex (the ULK1 kinase complex in mammals) and subsequently the formation of a liquid-droplet, pre-autophagosomal structure [33,34]. Nutrient starvation activates the ULK1 kinase complex, which phosphorylates ATG proteins, including Beclin 1 [35], ATG14 [36,37], and ATG9 [38], and contributes to the initiation of autophagosome formation [22,32]. On the other hand, ULK1 phosphorylates substrates that are

285 not directly involved in autophagosome formation, such as SEC16A [39], glycolytic enzymes [40], and STING [41]. p62 is also in this category, and it is closely involved in the LLPS, the p62 body formation [42]. In this study, we showed that ULK1 localized to p62 bodies (Fig. 2) and phosphorylated Ser349 of p62 (Fig. 1), the latter of which is required for KEAP1 localization and retention to p62 bodies and subsequent NRF2 activation (Figs. 3 and 4). Thus, ULK1

290 modulates the formation and degradation of p62 bodies and also plays a role in the antioxidative-stress response.

When does ULK1 phosphorylate p62? Since ULK1 was localized in p62 bodies both *in vitro* and *in vivo* (Fig. 2), it is plausible that ULK1 phosphorylates Ser349 of p62 located in p62 bodies. Indeed, we hardly observed phosphorylation of the p62$^{K7A\ D69A}$ mutant, which

295 is not capable of LLPS (data not shown). How does ULK1 recognize p62 bodies? Our HS-AFM showed that the p62 homodimer directly bound to ULK1 via dynamic IDR-IDR and IDR-globular domain interactions (Fig. 1f). It is known that IDRs specifically interact with multiple target molecules through a binding mode called "coupled folding and binding" [43]. This binding mode may facilitate conformational changes and phosphorylation of large

300 numbers of p62 molecules in p62 bodies, because substitutions between IDRs that bind to target molecules occur very rapidly [44]. With the phosphomimetic p62 mutant p62^{S349E}, influx of KEAP1 into p62 bodies predominated over efflux (Fig. 4d and e). The coexpression of p62^{S349E} and KEAP1 in *p62 KEAP1* double-knockout Huh-1 cells reduced the circularity of p62 bodies compared to the expression of p62^{S349E} alone (Fig. 4a and b), and also decreased

305 the fluidity of KEAP1 molecules within p62 bodies (Fig. 4f). When the sequestration of

KEAP1 within p62 bodies surpasses a certain threshold level, these bodies convert from liquid-like to gel-like droplets. What does this mean? Since autophagy is known to target gel-like rather than liquid-like droplets [15,45,46], it is possible that incorporation of a certain number of KEAP1 molecules into p62 bodies changes them into gel-like aggregates and

310   enhances autophagic degradation. This is consistent with two findings: adding KEAP1 to p62 condensates consisting of p62^{S349E} resulted in amorphous aggregates *in vitro* (Fig. 4c), and *p62*$^{S351E/+}$ mice had reduced levels of not only Ser403-phosphorylated p62 representing p62 bodies but also KEAP1 (Fig. 5f). Once p62 bodies are degraded by autophagy, the interaction between Ser349-phosphorylated p62 and KEAP1 should be suppressed because

315   Ser349 phosphorylation of p62 occurs mainly in p62 bodies. As a result, KEAP1 remains in the cytoplasm, and NRF2 is degraded. In other words, the retention of KEAP1 in p62 bodies above a threshold level is thought to suppress NRF2 activation in a feedback regulation process.

      Nrf2$^{-/-}$ mice grow normally and are fertile [47], though they are susceptible to oxidative

320   stress and reactive electrophiles [17]. In addition, they show tooth decolorization due to defective iron transport in the enamel [48], which makes them easily distinguishable from wild-type and heterozygous mice. *p62*$^{S351A/S351A}$, the phosphodefective *p62* knock-in mice in which p62-mediated NRF2 activation should be impaired, were also fertile and did not differ from wild-type mice for 1 year, at least under specific pathogen-free conditions (Supplementary

325   Fig. S7). However, their incisors were brownish-yellow, in contrast to the greyish white incisors in *Nrf2*-deficient mice (data not shown), indicating that *p62*$^{S351A/S351A}$ mice retain NRF2 activity. p62-mediated NRF2 activation was not required for development or survival, at least under steady-state conditions. The redox-independent antioxidative stress response might have an anti-aging effect since p62 bodies are thought to increase when the activities

330   of both autophagy-lysosomes and the ubiquitin-proteasome system decrease with aging. Further research is needed to determine whether the redox-independent stress response is activated with aging, and if so, which tissues are affected.

      In sharp contrast to *p62*$^{S351A/S351A}$ mice, the phosphomimetic *p62* knock-in mice *p62*$^{S351E/+}$, in which p62-mediated NRF2 activation is persistently activated, showed severe

335   phenotypes. The mice had impaired nutritional intake due to hyperkeratosis in the esophagus and forestomach, which led to malnutrition and dehydration (Fig. 5). This represented almost a phenocopy of *Keap1*-deficient mice, which exhibit hyperactivation of NRF2 and show hyperkeratosis in the esophagus and forestomach [31]. One difference is that *p62*$^{S351E/+}$ mice do not develop skin hyperkeratosis, which is observed in *Keap1*-knockout mice [31]. Why does

340   constant activation of NRF2, which has an inherently cytoprotective role, cause a severe

phenotype? The esophagus and stomach are exposed to a variety of toxic foods and drinks. This may cause wounds that require NRF2 for healing, and a redox-independent p62-mediated pathway may be at work. Meanwhile, the healing of skin wounds may be mediated by redox-dependent NRF2 activation [49]. It is plausible that transient activation of NRF2 in

345   response to toxicity, whether redox-dependent or redox-independent, is important for biological defense, and that persistent activation leads to excessive defense responses (*e.g.*, excessive keratinization). In the case of redox-independent stress response, the transient activation would be regulated by phosphorylation, dephosphorylation, and autophagic degradation of p62 body.

350   In conclusion, we showed for first time that the redox-independent NRF2 activation pathway, which is mediated by p62 bodies and their phosphorylation, is physiologically important.

Methods

Cell culture

355   Huh-1 cells (JCRB0199, NIBIOHN) were cultured in Dulbecco's modified Eagle's medium containing 10% fetal bovine serum, 5 U/mL penicillin, and 50 μg/mL streptomycin. For overexpression experiments, Huh-1 cells were transfected using Lipofectamine 3000 (L3000015, Thermo Fisher Scientific, Waltham, MA, USA). Huh-1 cells were authenticated

360   using the STR profile and tested for mycoplasma contamination.

Mice

To generate $p62^{S351A}$ knock-in mice, CRISPR RNA (crRNA) was designed to recognize the target site (5'-ACTGGAGTTCACCTGTAGAT-3'). The synthetic crRNAs (Alt-R CRISPR-

365   Cas9 crRNA), trans-activating CRISPR RNA (tracrRNA) (Alt-R CRISPR-Cas9 tracrRNA), and Cas9 protein (Alt-R S.p. Cas9 Nuclease V3) were purchased from Integrated DNA Technologies, Inc. (IDT; Coralville, IA, USA). The 120-mer single-stranded oligodeoxynucleotide (ssODN) carrying the intended base substitutions (TCT to GCC) was synthesized by Eurofins Genomics K.K. (Tokyo, Japan). The CRISPR/Cas9 solution was

370   prepared as previously described [50], with minor modifications. Briefly, lyophilized crRNAs and tracrRNA were resuspended in nuclease-free duplex buffer (IDT) to a concentration of 240 μM. Equal volumes of crRNA and tracrRNA were combined, heated at 95°C for 5 min, and then placed in room temperature (RT) for about 10 min to allow formation of crRNA-tracrRNA duplex. Lyophilized ssODN was resuspended in nuclease-free water to a

375   concentration of 4 mg/mL. crRNA-tracrRNA duplex was mixed with Cas9 protein to form a

ribonucleoprotein complex, and then mixed with ssODN in Opti-MEM (Thermo Fisher Scientific). The final concentrations of Cas9 protein, crRNA-tracrRNA duplex, and ssODN were 1 μg/mL, 30 μM, and 1mg/mL, respectively. To induce CRISPR/Cas9-mediated mutation, we applied a method called improved genome editing via oviductal nucleic acid

380   delivery (i-GONAD) [50]. Approximately 1.5 mL of CRISPR/Cas9 solution was injected into the oviductal lumens of female C57BL/6N mice on day 0.7 of pregnancy. Immediately after the injection, the oviduct regions were grasped with a tweezer-type electrode (catalog no. CUY652-3; Nepa Gene Co., Ltd., Chiba, Japan) and then electroporated using the NEPA21 square-wave pulse generator (Nepa Gene). The electroporation parameters used were

385   previously described [50]. Pregnant female mice were allowed to deliver their pups. Biopsies of pup tails were performed for genomic DNA isolation, and mutations were validated by sequencing of PCR products amplified from genomic DNAs.

To generate $p62^{S351E}$ knock-in mice using mouse embryonic stem (mES) cells, we applied the recently developed prime editing system [30]. Details of the methods for

390   establishment of edited mES cells will be published elsewhere (Manabu Abe, et al). Briefly, we designed prime-editing guide RNA (pegRNA) containing the following sequences: spacer sequence, 5'-GACUGGAGUUCACCUGUAGA-3'; reverse transcription template, 5'-GUGGACCCAGAG-3'; primer-binding site, 5'-ACAGGUGAACUCC-3'. The CAG promoter-driven prime editor 2 (PE2) and the U6 promoter-driven pegRNA expression

395   vectors were originally constructed using pCMV-PE2-P2A-GFP (#132776, Addgene) and the hU6-sgRNA plasmid [51]. These vectors were co-transfected into RENKA4, a C57BL/6N-derived mES cell line, using Lipofectamine 3000 (Thermo Fisher Scientific). Knock-in mutations in transfected mES clones were validated by sequencing of PCR products amplified from genomic DNAs. Culture of mES cells and generation of chimeric mice were

400   carried out as previously described [52].

Purification of recombinant protein

mCherry-p62, mCherry-p62 mutants, SNAP-KEAP1, and SNAP-8xUb were prepared as described previously [15]. The gene encoding 8xUb was purchased from GenScript, New

405   Jersey,USA. Purified proteins were stored at −80 °C until use.

Recombinant SNAP-Atg1 proteins were prepared as described previously [34]. To construct the expression plasmid encoding TwinStrep-CS-SNAP-ULK1-His6 (CS; HRV 3C protease recognition site), the genes and pCAG-neo vector (FUJIFILM Wako Pure Chemical Corporation) were amplified by PCR. The PCR fragments were assembled using NEBuilder

410   HiFi DNA Assembly Master Mix (New England BioLabs (NEB), Ipswich, MA). The

construct was subjected to sequencing analysis to confirm its identity and transfected into Expi293 GnTI− cells using Screen *F*ect™ UP-293 (FUJIFILM Wako Pure Chemical Corporation). The cells were collected after 5 days and sonicated in lysis buffer (50 mM Tris-HCl [pH 8.0], 300 mM NaCl, 2 mM $MgCl_2$, 1% Triton X-100, 10% glycerol, 1 mM

415   TCEP, 1x protease inhibitor cocktail (Nacalai Tesque, Kyoto, Japan)) on ice and centrifuged at 16,000 *g* for 40 min at 4 °C. The supernatant was purified with a Strep-Tactin®XT resin column (IBA Lifesciences Göttingen, Germany). The protein was eluted with 20 mM Tris-HCl (pH 8.0), 500 mM NaCl, 50 mM biotin and concentrated using Vivaspin 500 (Cytiva, Massachusetts, USA).

420

HS-AFM

The procedure for HS-AFM observation was described previously [53]. HS-AFM images were acquired in tapping mode using a sample-scanning HS-AFM instrument (MS-NEX, Research Institute of Biomolecule Metrology Co., Ltd., Ibaraki, Japan). We used cantilevers

425   measuring ~7 µm long, ~2 µm wide, and ~0.08 µm thick with electron beam-deposited (EBD) tips (tip radius < 10 nm) (USC-F1.2-k0.15, NanoWorld, Neuchâtel, Switzerland). Their resonant frequency and spring constant were 1.2 MHz in air and 0.15 N/m, respectively. Imaging conditions were as follows: scan size, 120×120 nm^2 (Fig. 2f, Fig. S3a, b) or 150×150 nm^2 (Fig. S3c); pixel size, 100×100 pixels (Fig. 2f, Fig. S3a-c); imaging

430   rate, 8.33 frames/sec (Fig. 2f, Fig. S3a) or 6.67 frames/s (Fig. S3b,c). Imaging was performed at 23 °C. HS-AFM images were viewed and analyzed using the Kodec4.4.7.39 [54] and ImageJ software systems.

Sample preparation for HS-AFM imaging

435   For imaging of SNAP-ULK1 and p62_268–440, SNAP-ULK1 (50 nM) or p62_268–440 (10 nM) was deposited onto freshly cleaved mica glued to the top of a glass stage (diameter, 1.5 mm; height, 2 mm). After incubation for 3–5 min, the mica was rinsed and immersed in the liquid cell containing ~90 µL of imaging buffer A (20 mM NaCl, 20 mM HEPES-NaOH [pH 7.5], 1 mM $MgCl_2$, 0.1 mM ATP) or imaging buffer B (20 mM NaCl, 20 mM HEPES-NaOH

440   [pH 7.5], 1 mM $MgCl_2$), respectively. For imaging of p62_268–440 with SNAP-ULK1 or SNAP-ATG1, 25 nM p62_268–440 and 50 nM SNAP-ULK1 or 10 nM p62_268–440 and 5 nM SNAP-ATG1 in imaging buffer A were mixed in a 0.5-mL tube. The mixed protein solution was deposited onto freshly cleaved mica and incubated for 3–5 min. After rinsing with imaging buffer A, the mica was immersed in ~90 µL of imaging buffer A.

445

In vitro kinase assay

Purified p62 (268–440aa), p62 (320–440aa) or mCherry-p62 was incubated with purified SNAP-Atg1 or SNAP-ULK1 in kinase buffer (20 mM Tris-HCl [pH 7.5], 150 mM NaCl, 0.5 mM MgCl$_2$, 0.1 mM DTT) containing 200 μM of ATP per reaction for 30 min at 37 °C. The reaction was terminated by adding LDS sample buffer (NP0007, Thermo Fisher Scientific) and subjected to SDS-PAGE followed by immunoblot analyses with p62 Ser349-[20], Ser403-(GTX128171, GeneTex), and Ser407-[8] specific antibodies.

In vitro LLPS assay

For the *in vitro* LLPS assay, fluorescence observation was performed on glass-bottom dishes (MatTek, Massachusetts, USA) coated with 0.3% (w/v) bovine serum albumin using an FV3000RS confocal laser-scanning microscope (Olympus, Tokyo, Japan). Lasers with wavelengths of 488, 561, and 640 nm were used for excitation of Alexa Fluor 488, mCherry, and Alexa Fluor 649, respectively. To observe p62-8xUb condensates, mCherry-p62 wild-type (WT) or mCherry-p62 mutant was mixed with SNAP(649)-8xUb (SNAP-8xUb labeled with SNAP-Surface 649). Each final protein concentration was 10 μM. To observe p62-8xUb condensates in the presence of ATG1 or ULK1, SNAP(488)-ATG1 or SNAP(488)-ULK1 (SNAP-ATG1 / ULK1 labeled with SNAP-Surface Alexa Fluor 488) was premixed with mCherry-p62WT / p62S403_S407E before mixing with SNAP(649)-8xUb. The final concentrations of SNAP(488)-Atg1 / ULK1, SNAP(649)-8xUb, and mCherry-p62WT / p62S403E_S407E were 0.2 μM, 10 μM, and 10 μM, respectively. To observe p62-8xUb condensates in the presence of KEAP1, SNAP(488)-KEAP1 (SNAP-KEAP1 labeled with SNAP-Surface Alexa Fluor 488) was premixed with mCherry-p62 mutant before mixing with SNAP(649)-8xUb. The final concentrations of SNAP(488)-KEAP1, SNAP(649)-8xUb, and mCherry-p62 mutants were 5 μM, 10 μM, and 10 μM, respectively. The buffer solutions used for the *in vitro* LLPS assay were 200 mM NaCl, 20 mM HEPES-NaOH (pH 7.5), 10% glycerol, and 1 mM TCEP. Each mixed solution was incubated for 50 min at ~23 °C before imaging.

The % area of p62 condensates (the sum of the areas of p62 condensates divided by the total area (106.7 μm × 106.7 μm)) (Fig. 2a) was calculated using the "analyze particles" tool of ImageJ software. Statistical analysis was performed by Welch's *t*-test.

Immunoblot analysis

Cells were lysed in ice-cold TNE buffer (50 mM Tris-HCl [pH 7.5], 150 mM NaCl, 1 mM EDTA) containing 1% Triton X-100 and cOmplete EDTA-free protease inhibitor cocktail

(5056489001, Roche). After centrifugation twice at 15,000 *g* for 10 min, the supernatant was collected as the cell lysates. Protein concentrations were determined by bicinchoninic acid (BCA) protein assay (23225, Thermo Fisher Scientific). The lysate was boiled in LDS sample buffer, and the samples were separated by SDS-PAGE and then transferred to

485   polyvinylidene difluoride membranes. For gene knockdown, cells were transfected with siGENOME siRNA targeting *ULK1* (D-005049-01-0005; 5'-CCUAAAACGUGUCUUAUUU-3', D-005049-02-0005; 5'-ACUUGUAGGUGUUUAAGAA-3', D-005049-03-0005; 5'-GGUUAGCCCUGCCUGAAUC-3', Horizon Discovery, United Kingdom) and *ULK2* (MQ-

490   005396-01-0002; mixtures of sequences 5'-UAAAGGAACUUCAGCAUGA-3', 5'-GUGGAGACCUCGCAGAUUA-3', 5'-GAAGAACAGUCGAAAGAUUA-3', 5'-GCAGACGUGCUUCAAAUGA-3', Horizon Discovery) or a non-targeting control siRNA (siGENOME Non-Targeting siRNA; mixtures of sequences 5'-UAGCGACUAAACACAUCAA-3', 5'-UAAGGCUAUGAAGAGAUAC-3', 5'-

495   AUGUAUUGGCCUGUAUUAG-3', and 5'-AUGAACGUGAAUUGCUCAA-3', Horizon Discovery) using DharmaFECT1 (T-2002, Horizon Discovery) and lysed 96 h after transfection in TNE buffer containing 1% SDS. Antibodies against p62 (610832, BD Biosciences, New Jersey, USA), Ser403-phosphorylated p62 (GTX128171, GeneTex California, USA), Ser349-phosphorylated p62 [20], Ser405-phosphorylated p62 [8], ULK1 (8054,

500   Cell Signaling Technology, Massachusetts, USA), ULK2 (A15244, ABclonal, TE Huissen, Netherlands), FIP200 (17250-1-AP, Proteintech Group, Illinois, USA), and NRF2 (H-300; Santa Cruz Biotechnology, California, USA) were used as primary antibodies. Blots were then incubated with horseradish peroxidase-conjugated secondary antibody (Goat Anti-Mouse IgG (H + L), 115-035-166, Goat Anti-Rabbit IgG (H + L) 111-035-144, and Goat

505   Anti-Guinea Pig IgG (H + L), all from Jackson ImmunoResearch, Pennsylvania, USA) and visualized by chemiluminescence.

Immunofluorescence analysis

Huh-1 cells on coverslips were washed with PBS and fixed with 4% paraformaldehyde

510   (PFA) for 15 min at RT, permeabilized with 0.1% Triton X-100 in PBS for 5 min, and blocked with 0.1% (w/v) gelatin (G9391, Sigma-Aldrich, Darmstadt, Germany) in PBS for 20 min. Then, cells were incubated with primary antibodies in the blocking buffer for 1 h, washed with PBS, and incubated with secondary antibodies for 1 h. Antibodies against p62 (610832, BD Biosciences), S403-phosphorylated p62 (GTX128171, GeneTex), S349-

515   phosphorylated p62 [20], KEAP1 (10503-2-AP, Proteintech), and ULK1 (8054, Cell Signaling

Technology) were used as primary antibodies. Goat anti-Mouse IgG (H + L) Highly Cross-Adsorbed Secondary Antibody, Alexa Fluor 647 (A21236, Thermo Fisher Scientific) and Goat anti-Rabbit IgG (H + L) Cross-Adsorbed Secondary Antibody, Alexa Fluor 488 (A11008, Thermo Fisher Scientific) were used as secondary antibodies. Nuclei were stained

520 with Hoechst 33342 (62249, Thermo Fisher Scientific). Cells were imaged using the FV1000 confocal laser-scanning microscope with FV10-ASW 04.01 (Olympus) and a UPlanSApo ×60 NA 1.40 oil objective lens. Contrast and brightness of images were adjusted using Photoshop 2021v25.0 (Adobe, California, USA). The number, size, and circularity of p62-positive punctae in each cell and the mean fluorescence intensity of each signal on p62-

525 positive punctae were quantified using a Benchtop High-Content Analysis System (CQ1, Yokogawa Electric Corp., Tokyo, Japan) and CellPathfinder software (Yokogawa Electric Corp.).

Correlative light and electron microscopic analysis

530 Huh-1 cells on coverslips etched with 150-µm grids (CS01885, Matsunami Glass Ind. Osaka, Japan) were transfected with pMRX-IP-GFP-ULK1 or pMRX-IP-GFP-ULK2. After 24 h, cells were fixed with 2% PFA–0.1% glutaraldehyde (GA) in 0.1 M PB (pH 7.4). Then, phase-contrast and fluorescence images were obtained using a confocal microscope (FV1000). After image acquisition, the cells were fixed again with 2% PFA and 2% GA in

535 0.1 M PB (pH 7.4), processed according to the reduced-osmium method [55], and embedded in Epon812. Areas containing cells of interest were trimmed, cut as serial 80-nm sections, and observed using an electron microscope (EM; JEM1400; JEOL). Light microscopy and EM images were aligned according to three p62 bodies using Photoshop CS6 (Adobe).

540 **Histological analyses**

Mouse livers were excised, cut into small pieces, and fixed by immersion in 4% PFA–4% sucrose in 0.1 M PB, pH 7.4. After rinsing, they were embedded in paraffin for immunostaining. Paraffin sections of 3-µm thickness were prepared and processed for HE staining or IHC. For IHC, antigen retrieval was performed for 20 min at 98 ˚C using a

545 microwave processor (MI-77, AZUMAYA, Japan) in 1% immunosaver (Nissin EM, Japan). Sections were blocked and incubated for 2 days at 4 ˚C with the following primary antibodies: rabbit polyclonal antibody against NQO1 (Abcam), followed by N-Histofine simple stain mouse MAX PO kit (NICHIREI BIOSCIENCES, Tokyo, Japan) using 3,39-diaminobenzidine. Images of the stained specimens were acquired with a microscope (BX51,

550 Olympus) equipped with a cooled CCD camera system (DP-71, Olympus).

FRAP and FLIP assays

p62/*KEAP1* double-knockout Huh-1 cells expressing GFP-p62^{S349E} or GFP-p62^{S349A} in a doxycycline treatment-dependent manner were generated using a reverse tet-regulated

555   retroviral vector, as previously reported. To induce the expression of GFP-p62^{S349E} or GFP-p62^{S349A}, the cells were treated with 50 ng/mL of doxycycline (Dox, Sigma-Aldrich) for 24 h. Thereafter, mCherry-KEAP1 was transfected with Lipofectamine 3000 (Thermo Fisher Scientific) and cultured for 24 h. In FRAP assays, GFP-p62 bodies that were positive for mCherry-KEAP1 were bleached using a laser intensity of 10% at 488 nm, and then the

560   fluorescence recovery of mCherry was recorded. In FLIP assays, almost 80% of the total cell area was set as the region of interest for photobleaching (excitation output level: 10% at 561 nm; iterations: 3–5) using FV31S-SW software (Olympus), and then the fluorescence loss of mCherry-KEAP1 in GFP-p62^{S349E} or GFP-p62^{S349A} bodies was recorded. The fluorescence intensity of mCherry-KEAP1 within the p62 bodies in the photobleaching area recovered to

565   32% at 15 min after photobleaching and reached equilibrium. Therefore, the fluorescence intensity of mCherry-KEAP1 within the p62 bodies in the non-photobleaching area was measured at 30 min after fluorescence loss. Olympus FV31S-SW software (version: 2.4.1.198) and cellSens Dimension Desktop 3.2 (Build 23706) was used for image collection and analysis. The mobile fraction was calculated from 10 measurements by the following

570   equation: $Mf = (F\infty-F0)/(Fi-F0)$, where Mf is the mobile fraction, F∞ is the fluorescence intensity after full recovery (plateau), Fi is the initial fluorescence intensity prior to bleaching, and F0 is the fluorescence intensity immediately after bleaching. The half-time (*t50*) of fluorescence recovery was calculated from 10 measurements by curve fitting using the one-phase decay model of GraphPad PRISM 9 (GraphPad Software, California, USA).

575

RNA sequencing (RNA-seq)

Total RNA from livers of *p62$^{+/+}$* and *p62$^{S351E/+}$* mice at P19 was extracted using the RNeasy Mini Kit (Qiagen, Hulsterweg, Netherland). Ribosomal RNA was depleted using a NEBNext rRNA Depletion Kit (NEB). For sequencing, a cDNA library was synthesized using the

580   NEBNext Ultra II RNA Library Prep Kit for Illumina (NEB). Sequencing was performed on a NextSeq 500 sequencer (Illumina, San Diego, CA, USA) with 75-bp single-end reads. Resulting reads were mapped to the UCSC (University of California, Santa Cruz, CA, USA) mm10 reference genome using the Spliced Transcripts Alignment to a Reference (STAR) Aligner. The n umber of reads was calculated using RNA-Seq by Expectation Maximization

585   (RSEM), and differentially expressed genes (DEGs) between $p62^{+/+}$ and $p62^{S351E/+}$ mice were analyzed by DESeq2. DEGs were visualized by volcano plots.

Quantitative real-time PCR (qRT-PCR)

cDNAs were synthesized with 1 μg of total RNA using FastGene Scriptase Basic cDNA

590   Synthesis (NE-LS62, NIPPON Genetics, Tokyo, Japan). qRT-PCR was performed with TaqMan® Fast Advanced Master Mix (444556, Thermo Fisher Scientific) on a QuantStudio™ 6 Pro (A43180, Thermo Fisher Scientific). Signals were normalized against *Gusb* (β-glucuronidase). Predesigned TaqMan Gene Expression Assays, including primer sets and TaqMan probes (Gusb; Mm01197698_m1, Nqo1; Mm01253561_m1, Ugdh;

595   Mm00447643_m1 and Gstm1; Mm00833915_g1, GAPDH; Hs02786624_g1, NQO1; Hs00168547_m1, UGDH; Hs01097550_m1, GCLC; Hs00155249_m1, SOD1; Hs00533490_m1, SQSTM1; Hs00177654_m1) were purchased from Thermo Fisher Scientific.

600   **Statistical analysis**

Statistical analyses were performed using the unpaired *t*-test (Welch *t*-test), Tukey's test or Šidák's multiple comparison test after one-way ANOVA. GraphPad PRISM 9 (GraphPad Software) was used for the statistical analyses. All tests were two-sided, and P values of < 0.05 were considered statistically significant.

605   **Resources table**

REAGENT or RESOURCE	SOURCE	IDENTIFIER
Antibodies		
Guinea pig polyclonal anti-p62/ SQSTM1 (C-terminus)	Progen Biotechnik	Cat#GP62-C; RRID: AB_2687531
Mouse monoclonal anti-p62 Ick ligand	BD Biosciences	Cat#610833; RRID: AB_398152
Rabbit polyclonal anti-p62 (pSer403)	Gene Tex	Cat#GTX128171; RRID: AB_2885723
Rabbit polyclonal anti-p62 (pSer349)	[20]	N/A
Rabbit polyclonal anti-p62	MBL	Cat#PM045; RRID: AB_1279301
Mouse monoclonal anti-p62	Abnova	Cat#H00008878-M01; RRID: AB_1507408
Rabbit polyclonal anti-KEAP1	Proteintech	Cat#10503-2-AP; RRID: AB_2132625
Rabbit monoclonal anti-ULK1 (D8H5)	Cell Signaling Technology	Cat#8054; RRID: AB_11178668

Rabbit polyclonal anti-ULK2	ABclonal	Cat#NBP-89866; RRID: AB_11009420
Rabbit monoclonal anti-ATG13 (E1Y9V)	Cell Signaling Technology	Cat#13468; RRID: AB_2797419
Rabbit polyclonal anti-ATG13 (pSer318)	Rockland	Cat# 600-401-C49; RRID: AB_11179920
Rabbit polyclonal anti-NRF2 (H-300)	Santa Cruz Biotechnology	Cat#sc-13032; RRID: AB_2263168
Rabbit polyclonal anti-RB1CC1	Proteintech	Cat#17250-1-AP; RRID: AB_10666428
Mouse monoclonal anti-β-actin	Sigma-Aldrich	Cat#A1978; RRID: AB_476692
Mouse monoclonal anti-GAPDH (6C5)	Santa Cruz Biotechnology	Cat#sc-32233; RRID: AB_627679
Mouse monoclonal anti-DDDDK-tag	MBL	Cat#M185-3L; RRID: AB_11123930
Rabbit polyclonal anti-GFP	MBL	Cat#598; RRID: AB_591819
Rabbit polyclonal anti-NQO1	Abcam	Cat#ab9085; RRID: AB_2251526
Rabbit polyclonal anti-UGDH	Abcam	Cat#ab155005
Alexa Fluor Plus 488-conjugated anti-mouse IgG	Thermo Fisher Scientific	Cat#A32766; RRID: AB_2762823
Alexa Fluor 488-conjugated anti-rabbit IgG	Thermo Fisher Scientific	Cat#A11034; RRID: AB_2576217
Alexa Fluor Plus 594-conjugated anti-mouse IgG	Thermo Fisher Scientific	Cat#A32744; RRID: AB_2762826
HRP-conjugated goat polyclonal anti-mouse IgG	Jackson ImmunoResearch Laboratories	Cat#115-035-166; RRID: AB_2338511
HRP-conjugated goat polyclonal anti-rabbit IgG	Jackson ImmunoResearch Laboratories	Cat#111-035-144; RRID: AB_2307391
HRP-conjugated goat polyclonal anti-guinea pig IgG	Jackson ImmunoResearch Laboratories	Cat#106-035-003; RRID: AB_2337402
Bacterial and Virus Strains		
E. coli BL21 (DE3)	Funakoshi	Cat#DS250
E. coli DH5α	Thermo Fisher Scientific	Cat#EC0112
Chemicals		
Lipofectamine 3000 Transfection Reagent	Thermo Fisher Scientific	Cat#L3000015
Lipofectamine RNAiMAX Transfection Reagent	Thermo Fisher Scientific	Cat#13778150
Lipofectamine LTX Reagent with PLUS Reagent	Thermo Fisher Scientific	Cat#15338100
DNase I	Takara Bio	Cat#2270A
Anti-GFP (Green Fluorescent Protein) mAb-Agarose	MBL	Cat#D153-8
Glutathione Sepharose 4B	GE Healthcare	Cat#17-0756-05

PreScission Protease	Cytiva	Cat#27084301
One Step CBB	BIO CRAFT	Cat#CBB-1000
Bafilomycin A_1	KOM	Cat#BVT-0252-M001
Isopropyl β-D-thiogalactopyranoside	Nacalai Tesque	Cat#19742-94
cOmplete EDTA-free (protease inhibitor cocktail)	Roche Applied Science	Cat#05056489001
PhosSTOP (phosphatase inhibitor cocktail)	Roche Applied Science	Cat#4906845001
Polyvinylpyrrolidone	Sigma-Aldrich	Cat#PVP10
Experimental Models: Cell Lines		
Huh-1	RIKEN	Cat#JCRB0199; RRID: CVCL_2956
Huh-1 *p62* KO	[20]	N/A
Huh-1 *FIP200* KO	This study	N/A
Huh-1 *p62, KEAP1* DKO	This study	N/A
Huh-1 *ULK1* KO	This study	N/A
HEK293T	ATCC	Cat#CRL-3216
PlatE	Cell BIOLABS	Cat#RV-101
Experimental Models: Organisms/Strains		
Mouse: *p62*$^{S351A/+}$	This study	N/A
Mouse: *p62*$^{S351A/S351A}$	This study	N/A
Mouse: *p62*$^{S351E/+}$	This study	N/A
Recombinant DNA		
pGEX6P-1	GE Healthcare	#28954648
pGEX6P-1-8xUb	Genscript	N/A
pGEX6P-KEAP1	This study	N/A
pGEX6P-mCherry-p62	This study	N/A
pGEX6P-mCherry-p62^{S349E}	This study	N/A
pGEX6P-mCherry-p62^{S403E}	This study	N/A
pEGFP-C2	Clontech	Cat#6083-1
pEGFP-C2-p62	This study	N/A
pEGFP-ULK1	This study	N/A
pRetroX-TetOne-Puro-EGFP-p62	This study	N/A
pRetroX-TetOne-Puro-EGFP-p62^{S349E}	This study	N/A
pRetroX-TetOne-Puro-EGFP-p62^{S349A}	This study	N/A
pRetroX-TetOne-Puro-EGFP-p62^{T350A}	This study	N/A
pIRES-puro-N3xFLAG	This study	N/A
pIRES-puro-N3xFLAG-ULK1	This study	N/A
pIRES-puro-N3xFLAG-ULK2	This study	N/A
Software and Algorithms		
ImageJ	Thermo Fisher Scientific	RRID: SCR_014477
CellPath Finder	[56]	RRID: SCR_002285

Evolution-Capt Edge	Yokogawa	N/A
FV10-ASW 04.01	Vilber Bio Imaging	N/A
Multi Gauge (version: 3.4)	Fuji Film	N/A
FV31S-SW (version: 2.4.1.198)	Olympus	N/A
Kodec	Olympus	N/A
Biomolecular AFM viewer-2.1	[54]	N/A
GraphPad Prism 9	[57]	N/A
Adobe Photoshop CS6	Adobe	N/A

Author Contributions

Y.I., N.N.N., and M.K. designed and directed the study. R.I., S.K., H.M., S.T., T.F., S.K-H., and Y.I. carried out the biochemical and cell biological experiments. S.K-H. generated knockout cell lines. D.N, Y.F., and N.N.N conducted high-speed AFM and in vitro LLPS analysis. R.A., E.L., and S.W. carried out histological analysis of mice. T.K. and M.N.

635   performed and analyzed RNA-seq analysis. H.A. provided intellectual support. N.N.N. and

M.K. wrote the manuscript. All authors discussed the results and commented on the

manuscript.

Conflicts of Interest

640   We declare that we have no competing financial interests.

Figure legends

Fig. 1 Molecular dynamics of ULK1 and p62

a Domain structures of ULK1, Atg1, and p62. KD, kinase domain; MIT, microtubule

645   interaction and transport domain; PB1, Phox1 and Bem1p domain; LIR, LC3-interacting

region; KIR, KEAP1-interacting region; UBA, ubiquitin-associated domain. **b** Predicted

three-dimensional structures of ULK1, Atg1, and p62 by Alphafold 2. **c** CBB staining of

purified p62 (268–440 aa), p62 (320–440 aa), SNAP-Atg1, and SNAP-ULK1. **d** Successive

HS-AFM images of p62_268–440 with SNAP-ULK1. Height scale: 0–3.5 nm; scale bar: 20

650   nm. **e** Schematics showing the observed molecular characteristics by HS-AFM. Grey spheres,

globular domains consisting of N-terminal KD and C-terminal MIT domain of ULK1; pink

spheres, globular domains consisting of C-terminal UBA domain of p62; blue thick solid

lines, IDRs. **f** *In vitro* kinase assay. Purified recombinant p62 (268–440 aa), p62 (320–440

aa) or mCherry-p62 was incubated for 20 min at 30 °C with purified SNAP-Atg1 or SNAP-

655   ULK1 in the presence or absence of ATP. Reactions were then terminated by adding LDS

sample buffer containing reducing agent, followed by immunoblot analysis with the

indicated antibodies. As positive and negative controls, Huh-1 cell lysates treated with or

without lambda protein phosphatase (λPP) were used. Data were obtained from three

independent experiments.

660

Fig. 2 Localization of ULK1 on p62 bodies

a *In vitro* formation of p62-8xUb condensates. 10 μM mCherry-p62 wild-type or mCherry-

p62$^{S403E\ S407E}$, 10 μM SNAP-8xUb labelled with Alexa Fluor 649. Scale bars: 20 μm. The

graph indicates the quantified area of p62 condensates formed by wild-type or mutant p62.

665   Data are means ± s.d of wild-type p62 and p62$^{S403E,\ S407E}$ condensates ($n = 4$). ***$p < 0.001$ as

determined by two-sided Welch's t-test. **b** *In vitro* formation of p62-8xUb-Atg1 or ULK1

condensates. 10 μM mCherry-p62 wild-type or mCherry-p62$^{S403E,\ S407E}$, 10 μM 8xUb labelled

with Alexa Fluor 649 and 0.2 μM SNAP-Atg1 or SNAP-ULK1 labelled with Alexa Fluor

488 were mixed and observed by fluorescence microscopy. Scale bars: 10 μm. **c**

670   Immunofluorescence microscopy. Wild-type, *FIP200*- or *ULK1*-knockout Huh-1 cells were immunostained with indicated antibodies. The mean fluorescence intensities of ULK1 on p62 bodies per cell were quantified in each genotype (n = 249 cells). Horizontal bars indicate medians, boxes the interquartile range (25th–75th percentiles) and whiskers 1.5× the interquartile range; outliers are plotted individually. Statistical analysis was performed by

675   Šidák's test after one-way ANOVA (***p < 0.001). Scale bars, 10 μm (main panels), 1 μm (inset panels). **d** Immunofluorescence microscopy. Wild-type and *FIP200*-knockout Huh-1 cells were transfected with GFP-ULK1 or GFP-ULK2 and immunostained with anti-p62 antibody. The mean fluorescence intensities of ULK1 on p62 bodies in each cell were quantified for each genotype (n = 79 cells). Horizontal bars indicate medians, boxes indicate

680   interquartile range (25th–75th percentiles), and whiskers indicate 1.5× interquartile range; outliers are plotted individually. Statistical analysis was performed by Welch's *t*-test. Scale bars, 10 μm (main panels), 1 μm (inset panels). **e** Correlative light and electron microscopy (CLEM) of Huh-1 cells expressing GFP-ULK1. Images of GFP-ULK1, corresponding electron micrograph (EM) images, and the merging of both (CLEM) are shown. Areas 1 and

685   2 are magnified in the bottom. Arrowheads indicate GFP-ULK1-positive p62 bodies. Scale bars, 5 μm (upper panel), 1 μm (lower panels), and 100 nm (insets of lower panels).

Fig. 3 Significance of p62 phosphorylation by ULK1 and ULK2

a Immunoblot analysis. Huh-1 cells were treated with or without 2.5 μM MRT68921 for 6 h,

690   and the cell lysates were subjected to immunoblot analysis with indicated antibodies. The asterisk indicates non-specific bands. Data shown are representative of three separate experiments. Bar graphs show the results of quantitative densitometric analysis of Ser349- or Ser403-phosphorylated p62 forms relative to total p62 (n = 3), and of Ser318-phosphorylated ATG13 relative to total ATG13 (n = 3). Data are means ± s.e. Statistical analysis was

695   performed by Welch's *t*-test. **b** Immunofluorescence microscopy. Huh-1 cells were treated with or without 2.5 μM MRT68921 for 6 h and immunostained with the indicated antibodies. The ratio of p62 (p-S403) to p62 on p62 bodies and the size and number of p62 bodies in each cell were quantified (n = 500 cells). Horizontal bars indicate medians, boxes indicate interquartile range (25-75th percentiles), and whiskers indicate 1.5× interquartile range;

700   outliers are plotted individually. Statistical analysis was performed by Welch's *t*-test (*p < 0.05, **p < 0.01, and ***p < 0.001). Scale bars, 10 μm (main panels), 1 μm (inset panels). **c** Immunofluorescence microscopy. Huh-1 cells were treated with or without 2.5 μM MRT68921 for 6 h and immunostained with the indicated antibodies. The ratio of p62 (p-S349) to p62 and the signal intensity of KEAP1 on p62 bodies in each cell were

705   quantified ($n = 500$ cells). Horizontal bars indicate medians, boxes indicate interquartile range (25th-75th percentiles), and whiskers indicate 1.5× interquartile range; outliers are plotted individually. Statistical analysis was performed by Welch's *t*-test (***p < 0.001). Scale bars, 10 μm (main panels), 1 μm (inset panels). **d** Gene expression of NRF2 targets. Total RNAs were prepared from Huh-1 cells treated with or without 2.5 μM MRT68921 for

710   6 h. Values were normalized against the amount of mRNA in non-treated Huh-1 cells. qRT-PCR analyses were performed as technical replicates on each biological sample. Data are means ± s.e. *p < 0.05, and ***p < 0.001 as determined by two-sided Welch's *t*-test.

Fig. 4 Dynamics of KEAP1 in p62 bodies

715   **a** Fluorescence microscopy. GFP-p62, GFP-p62^{S349E}, GFP-p62^{S349A}, or GFP-p62^{T350A} were co-transfected with mCherry or mCherry-KEAP1 into Huh1 *p62/KEAP1* double-knockout cells. Twenty-four hours after transfection, the fluorescence images were observed. **b** Circularity of p62 bodies. The circularity of p62 bodies in each cell was quantified ($n = 150$ cells). Horizontal bars indicate medians, boxes indicate interquartile range (25th–75th

720   percentiles), and whiskers indicate 1.5× interquartile range; outliers are plotted individually. Statistical analysis was performed by two-sided Welch's *t*-test. Scale bar: 2 μm. **c** *In vitro* formation of p62-KEAP1-8xUb condensates. 5 μM SNAP-KEAP1 labeled with SNAP-Surface Alexa Fluor 488 was premixed with 10 μM mCherry-p62 mutants before mixing with 10 μM SNAP(649)-8xUb. Scale bars: 20 μm. **d** FRAP analyses of mCherry-KEAP1

725   localized in p62 bodies comprised of GFP-p62^{S349E} or GFP-p62^{S349A}. The half-time of recovery (*t50*) and mobile fraction (MF) of mCherry-KEAP1 was measured by FRAP of whole p62 bodies ($n = 7$). Data are means ± s.d. Statistical analysis was performed by two-sided Welch's t-test. **e** FLIP analyses of mCherry-KEAP1 localized in p62 bodies comprised of GFP-p62^{S349E} or GFP-p62^{S349A}. The fluorescence loss of mCherry-KEAP1 in GFP-p62

730   bodies ($n = 14$) was measured 30 min after photobleaching over a large area of cells. **f** FRAP analyses of mCherry-KEAP1 localized in p62 bodies comprised of GFP-p62^{S349E} or GFP-p62^{S349A}. *t50* and MF of mCherry-KEAP1 were measured by FRAP of the central portions of p62 bodies ($n = 10$). Data are means ± s.d. Statistical analysis was performed by two-sided Welch's t-test.

735

Fig. 5 Physiological significance of p62 phosphorylation at S351 in mice

a External appearance of *p62$^{+/+}$* and *p62$^{S351E/+}$* mice at postnatal days (P) 12 and 15. **b, c** Body weight (g) (**b**) and liver weight (% of body weight) (**c**) of *p62$^{+/+}$* ($n = 4$ at P12, $n = 10$ at P15) and *p62$^{S351E/+}$* mice ($n = 4$). Data are means ± s.e. Statistical analysis was performed

740   by Tukey's test after one-way ANOVA. **d** RNA-seq analysis of livers of *p62*$^{+/+}$ and *p62*$^{S351E/+}$ mice at P19 (*n* = 3). Volcano plots of differentially expressed genes in *p62*$^{+/+}$ versus *p62*$^{S351E/+}$ mice (red points: FDR < 0.05 and log2FC > 1, blue points: FDR < 0.05 and log2FC < -1). Green points are the targets of transcription factor NRF2. **e** Gene expression of NRF2 targets. Total RNAs were prepared from mouse livers of *p62*$^{+/+}$ (*n* = 10) and *p62*$^{S351E/+}$

745   (*n* = 4) mice at P15. Data are means ± s.e. Statistical analysis was performed by Welch's *t*-test. **f** Immunoblot analysis of *p62*$^{+/+}$ (*n* = 7) and *p62*$^{S351E/+}$ (*n* = 3) mice at P19. Liver homogenates were subjected to immunoblot analysis with the indicated antibodies. Bar graphs show the results of quantitative densitometric analysis. Data are means ± s.e. Statistical analysis was performed by Welch's *t*-test. **g, h** Hematoxylin and eosin (HE)

750   staining (**g**) and immunohistochemical analysis of NQO1 (**h**) of livers from *p62*$^{+/+}$ and *p62*$^{S351E/+}$ mice at P19. Scale bars, XX μm. **i** Serum levels of aspartate aminotransferase (AST), alanine aminotransferase (ALT), glucose, total cholesterol, blood urea nitrogen (BUN), and creatinine from *p62*$^{+/+}$ (*n* = 4 at P12, *n* = 10 at P15) and *p62*$^{S351E/+}$ (*n* = 4) mice at P12 and P15 were measured. IU/l, international units/liter. Data are means ± s.e. Statistical

755   analysis was performed by Tukey's test after one-way ANOVA.

Supplementary Fig. S1 HS-AFM observation of SNAP-ULK1 and p62 (268–440 aa), and complex of SNAP-Atg1/p62 (268–440 aa)

a,b Successive HS-AFM images of SNAP-ULK1 (a) and p62_268–440 (b). Height scale: 0–

760   4.4 nm (a), 0–3.4 nm (b); scale bar: 20 nm (a,b). **c** Successive HS-AFM images of p62_268–440 with SNAP-Atg1. Height scale: 0–3.6 nm; scale bar: 30 nm. **d** Schematics showing the molecular characteristics determined by HS-AFM. Grey spheres, globular domains consisting of N-terminal KD and C-terminal MIT of Atg1; pink spheres, globular domains consisting of C-terminal UBA domain of p62; blue thick solid lines, IDRs.

765

Supplementary Fig. S2 Generation of *ULK1* knockout , *FIP200* knockout, and *p62*/*KEAP1* double-knockout cell lines

Immunoblot analysis. The indicated genotype cell lines were lysed, then subjected to SDS-PAGE followed by immunoblot analysis with the indicated antibodies. The asterisk indicates

770   non-specific bands.

Supplementary Fig. S3 An mTORC1 inhibitor has no effect on the phosphorylation level of p62 in Huh1

Immunoblot analysis. Huh-1 cells were treated with 250 nM Torin-1 for 6 h, and the cell
lysates were subjected to immunoblot analysis with the indicated antibodies. The asterisk
indicates non-specific bands. Data shown are representative of three or four separate
experiments. Bar graphs show the results of quantitative densitometric analysis of Ser349- or
Ser403-phosphorylated p62 forms relative to total p62 ($n = 4$), Thr389-phosphorylated
p70S6K relative to total p70S6K ($n = 3$), and Ser318-phosphorylated ATG13 relative to total
ATG13 ($n = 4$). Data are means ± s.e. Statistical analysis was performed by Šidák's test after
one-way ANOVA.

Supplementary Fig. S4 Effect of ULK1 and the ULK2 inhibitor ULK-101 on p62 phosphorylation

Immunoblot analysis. Huh-1 cells were treated with or without 7.5 μM ULK-101 for 6 h,
and the cell lysates were subjected to immunoblot analysis with the indicated antibodies. The
asterisk indicates non-specific bands. Data shown are representative of three separate
experiments. Bar graphs show the results of quantitative densitometric analysis of S349- or
S403-phosphorylated p62 forms relative to total p62 ($n = 3$), and of S318-phosphorylated
ATG13 relative to total ATG13 ($n = 3$). Data are means ± s.e. Statistical analysis was
performed by Welch's *t*-test.

Supplementary Fig. S5 *In vitro* formation of p62$^{S349E\_S403E\_S407E}$-8xUb condensates

10 μM mCherry-p62$^{S349E\_S403E\_S407E}$ was mixed with 10 μM SNAP-8xUb labeled with SNAP-
Surface 649. Scale bar: 20 μm.

Supplementary Fig. S6 Gross anatomy of the stomach of *p62$^{+/+}$* and *p62$^{S351E/+}$* mice

The forestomach of *p62^{S351E}* heterozygotes was obviously thickened compared with that of
wild-type mice.

Supplementary Fig. S7 Analysis of mice lacking p62 phosphorylation at S351

a External appearance of *p62$^{+/+}$*, *p62$^{S351A/+}$*, and *p62$^{S351A/S351A}$* mice at postnatal day (P) 19. **b,
c** Body weight (g) (**b**) and liver weight (% of body weight) (**c**) of *p62$^{+/+}$* ($n = 3$), *p62$^{S351A/+}$* ($n = 6$), and *p62$^{S351A/S351A}$* mice ($n = 3$) at P19. Data are means ± s.e. Statistical analysis was
performed by Tukey's test after one-way ANOVA. **d** Gene expression of NRF2 targets.
Total RNAs were prepared from mouse livers of *p62$^{+/+}$* ($n = 3$), *p62$^{S351A/+}$* ($n = 6$), and
p62$^{S351A/S351A}$ mice ($n = 3$) at P19. Data are means ± s.e. Statistical analysis was performed by
Tukey's test after one-way ANOVA. **e** Immunoblot analysis of *p62$^{+/+}$* ($n = 3$), *p62$^{S351A/+}$* ($n =$

810

6), and $p62^{S351A/S351A}$ mice ($n = 3$) at P19. Liver homogenates were subjected to immunoblot analysis with the indicated antibodies. Bar graphs show the results of quantitative densitometric analysis. Data are means ± s.e. Statistical analysis was performed by Tukey's test after one-way ANOVA. **f** Hematoxylin and eosin (HE) staining of livers from $p62^{+/+}$, $p62^{S351A/+}$, and $p62^{S351A/S351A}$ mice at P19. Scale bar, XX μm. **g** Serum levels of aspartate aminotransferase (AST), alanine aminotransferase (ALT), glucose, total cholesterol, blood

815

urea nitrogen (BUN), and creatinine from $p62^{+/+}$ ($n = 3$), $p62^{S351A/+}$ ($n = 6$), and $p62^{S351A/S351A}$ mice ($n = 3$) at P19 were measured. IU/l, international units/liter. Data are means ± s.e. Statistical analysis was performed by Tukey's test after one-way ANOVA.

Supplementary Movie S1

820

HS-AFM movie of SNAP-ULK1. The images were acquired at 5 fps. Height scale: 0–3 nm. Scale bar: 20 nm.

Supplementary Movie S2

HS-AFM movie of p62_268–440. The images were acquired at 5 fps. Height scale: 0–3 nm.

825

Scale bar: 20 nm.

Supplementary Movie S3

HS-AFM movie of p62_268–440 with SNAP-ULK1. The images were acquired at 5 fps. Height scale: 0–3 nm. Scale bar: 20 nm.

830

Supplementary Movie S4

HS-AFM movie of p62_268–440 with SNAP-Atg1. The images were acquired at 5 fps. Height scale: 0–3 nm. Scale bar: 30 nm.

835

Supplementary Movie S5

Representative time-lapse image of mCherry-KEAP1 after photobleaching of whole GFP-p62^{S349E} body (Scale bar: 2 μm).

Supplementary Movie S6

840

Representative time-lapse image of mCherry-KEAP1 after photobleaching of whole GFP-p62^{S349A} body (Scale bar: 2 μm).

Supplementary Movie S7

845   Representative time-lapse image showing fluorescence loss of mCherry-KEAP1 in GFP-p62^{S349E} bodies after photobleaching over a large area of cells (Scale bar: 20 µm).

Supplementary Movie S8

Representative time-lapse image of mCherry-KEAP1. The fluorescence loss of mCherry-KEAP1 in GFP-p62^{S349A} bodies after photobleaching at a large area of cells (Scale bar: 20

850   µm).

Supplementary Movie S9

Representative time-lapse image of mCherry-KEAP1 after photobleaching of the central portion of p62^{S349E} body (Scale bar: 2 µm).

855

Supplementary Movie S10

Representative time-lapse image of mCherry-KEAP1 after photobleaching of the central portion of p62^{S349A} body (Scale bar: 2 µm).

References

1. Alberti, S., and Hyman, A.A. (2021). Biomolecular condensates at the nexus of cellular stress, protein aggregation disease and ageing. Nat Rev Mol Cell Biol *22*, 196-213. 10.1038/s41580-020-00326-6.

2. Woodruff, J.B., Hyman, A.A., and Boke, E. (2018). Organization and Function of Non-dynamic Biomolecular Condensates. Trends Biochem Sci *43*, 81-94. 10.1016/j.tibs.2017.11.005.

3. Noda, N.N., Wang, Z., and Zhang, H. (2020). Liquid-liquid phase separation in autophagy. J Cell Biol *219*. 10.1083/jcb.202004062.

4. Sun, D., Wu, R., Zheng, J., Li, P., and Yu, L. (2018). Polyubiquitin chain-induced p62 phase separation drives autophagic cargo segregation. Cell Res *28*, 405-415. 10.1038/s41422-018-0017-7.

5. Zaffagnini, G., Savova, A., Danieli, A., Romanov, J., Tremel, S., Ebner, M., Peterbauer, T., Sztacho, M., Trapannone, R., Tarafder, A.K., et al. (2018). p62 filaments capture and present ubiquitinated cargos for autophagy. EMBO J *37*. 10.15252/embj.201798308.

6. Kirkin, V., and Rogov, V.V. (2019). A Diversity of Selective Autophagy Receptors Determines the Specificity of the Autophagy Pathway. Mol Cell *76*, 268-285. 10.1016/j.molcel.2019.09.005.

7. Faruk, M.O., Ichimura, Y., and Komatsu, M. (2021). Selective autophagy. Cancer Sci *112*, 3972-3978. 10.1111/cas.15112.

8. Lim, J., Lachenmayer, M.L., Wu, S., Liu, W., Kundu, M., Wang, R., Komatsu, M., Oh, Y.J., Zhao, Y., and Yue, Z. (2015). Proteotoxic stress induces phosphorylation of p62/SQSTM1 by ULK1 to regulate selective autophagic clearance of protein aggregates. PLoS Genet *11*, e1004987. 10.1371/journal.pgen.1004987.

9. Isogai, S., Morimoto, D., Arita, K., Unzai, S., Tenno, T., Hasegawa, J., Sou, Y.S., Komatsu, M., Tanaka, K., Shirakawa, M., and Tochio, H. (2011). Crystal structure of the ubiquitin-associated (UBA) domain of p62 and its interaction with ubiquitin. J Biol Chem *286*, 31864-31874. 10.1074/jbc.M111.259630.

10. Matsumoto, G., Wada, K., Okuno, M., Kurosawa, M., and Nukina, N. (2011). Serine 403 phosphorylation of p62/SQSTM1 regulates selective autophagic clearance of ubiquitinated proteins. Mol Cell *44*, 279-289. 10.1016/j.molcel.2011.07.039.

11. Pilli, M., Arko-Mensah, J., Ponpuak, M., Roberts, E., Master, S., Mandell, M.A., Dupont, N., Ornatowski, W., Jiang, S., Bradfute, S.B., et al. (2012). TBK-1 promotes autophagy-mediated antimicrobial defense by controlling autophagosome maturation. Immunity *37*, 223-234. 10.1016/j.immuni.2012.04.015.

12. Kehl, S.R., Soos, B.A., Saha, B., Choi, S.W., Herren, A.W., Johansen, T., and Mandell, M.A. (2019). TAK1 converts Sequestosome 1/p62 from an autophagy receptor to a signaling platform. EMBO Rep *20*, e46238. 10.15252/embr.201846238.

13. Turco, E., Witt, M., Abert, C., Bock-Bierbaum, T., Su, M.Y., Trapannone, R., Sztacho, M., Danieli, A., Shi, X., Zaffagnini, G., et al. (2019). FIP200 Claw Domain Binding to p62 Promotes Autophagosome Formation at Ubiquitin Condensates. Mol Cell *74*, 330-346 e311. 10.1016/j.molcel.2019.01.035.

14. Turco, E., Savova, A., Gere, F., Ferrari, L., Romanov, J., Schuschnig, M., and Martens, S. (2021). Reconstitution defines the roles of p62, NBR1 and TAX1BP1 in ubiquitin condensate formation and autophagy initiation. Nat Commun *12*, 5212. 10.1038/s41467-021-25572-w.

15. Kageyama, S., Gudmundsson, S.R., Sou, Y.S., Ichimura, Y., Tamura, N., Kazuno, S., Ueno, T., Miura, Y., Noshiro, D., Abe, M., et al. (2021). p62/SQSTM1-droplet serves as a platform for autophagosome formation and anti-oxidative stress response. Nat Commun *12*, 16. 10.1038/s41467-020-20185-1.

16.	Agudo-Canalejo, J., Schultz, S.W., Chino, H., Migliano, S.M., Saito, C., Koyama-Honda, I., Stenmark, H., Brech, A., May, A.I., Mizushima, N., and Knorr, R.L. (2021). Wetting regulates autophagy of phase-separated compartments and the cytosol. Nature *591*, 142-146. 10.1038/s41586-020-2992-3.

17.	Yamamoto, M., Kensler, T.W., and Motohashi, H. (2018). The KEAP1-NRF2 System: a Thiol-Based Sensor-Effector Apparatus for Maintaining Redox Homeostasis. Physiol Rev *98*, 1169-1203. 10.1152/physrev.00023.2017.

18.	Cuadrado, A., Rojo, A.I., Wells, G., Hayes, J.D., Cousin, S.P., Rumsey, W.L., Attucks, O.C., Franklin, S., Levonen, A.L., Kensler, T.W., and Dinkova-Kostova, A.T. (2019). Therapeutic targeting of the NRF2 and KEAP1 partnership in chronic diseases. Nat Rev Drug Discov *18*, 295-317. 10.1038/s41573-018-0008-x.

19.	Komatsu, M., Kurokawa, H., Waguri, S., Taguchi, K., Kobayashi, A., Ichimura, Y., Sou, Y.S., Ueno, I., Sakamoto, A., Tong, K.I., et al. (2010). The selective autophagy substrate p62 activates the stress responsive transcription factor Nrf2 through inactivation of Keap1. Nat Cell Biol *12*, 213-223. 10.1038/ncb2021.

20.	Ichimura, Y., Waguri, S., Sou, Y.S., Kageyama, S., Hasegawa, J., Ishimura, R., Saito, T., Yang, Y., Kouno, T., Fukutomi, T., et al. (2013). Phosphorylation of p62 activates the Keap1-Nrf2 pathway during selective autophagy. Mol Cell *51*, 618-631. 10.1016/j.molcel.2013.08.003.

21.	Kodera, N., Noshiro, D., Dora, S.K., Mori, T., Habchi, J., Blocquel, D., Gruet, A., Dosnon, M., Salladini, E., Bignon, C., et al. (2021). Structural and dynamics analysis of intrinsically disordered proteins by high-speed atomic force microscopy. Nat Nanotechnol *16*, 181-189. 10.1038/s41565-020-00798-9.

22.	Lin, M.G., and Hurley, J.H. (2016). Structure and function of the ULK1 complex in autophagy. Curr Opin Cell Biol *39*, 61-68. 10.1016/j.ceb.2016.02.010.

23.	Jakobi, A.J., Huber, S.T., Mortensen, S.A., Schultz, S.W., Palara, A., Kuhm, T., Shrestha, B.K., Lamark, T., Hagen, W.J.H., Wilmanns, M., et al. (2020). Structural basis of p62/SQSTM1 helical filaments and their role in cellular cargo uptake. Nat Commun *11*, 440. 10.1038/s41467-020-14343-8.

24.	Petherick, K.J., Conway, O.J., Mpamhanga, C., Osborne, S.A., Kamal, A., Saxty, B., and Ganley, I.G. (2015). Pharmacological inhibition of ULK1 kinase blocks mammalian target of rapamycin (mTOR)-dependent autophagy. J Biol Chem *290*, 11376-11383. 10.1074/jbc.C114.627778.

25.	Martin, K.R., Celano, S.L., Solitro, A.R., Gunaydin, H., Scott, M., O'Hagan, R.C., Shumway, S.D., Fuller, P., and MacKeigan, J.P. (2018). A Potent and Selective ULK1 Inhibitor Suppresses Autophagy and Sensitizes Cancer Cells to Nutrient Stress. iScience *8*, 74-84. 10.1016/j.isci.2018.09.012.

26.	Faruk, M.O., Ichimura, Y., Kageyama, S., Komatsu-Hirota, S., El-Gowily, A.H., Sou, Y.S., Koike, M., Noda, N.N., and Komatsu, M. (2021). Phase-separated protein droplets of amyotrophic lateral sclerosis-associated p62/SQSTM1 mutants show reduced inner fluidity. J Biol Chem *297*, 101405. 10.1016/j.jbc.2021.101405.

27.	Strom, A.R., Emelyanov, A.V., Mir, M., Fyodorov, D.V., Darzacq, X., and Karpen, G.H. (2017). Phase separation drives heterochromatin domain formation. Nature *547*, 241-245. 10.1038/nature22989.

28.	Ishikawa-Ankerhold, H.C., Ankerhold, R., and Drummen, G.P. (2012). Advanced fluorescence microscopy techniques--FRAP, FLIP, FLAP, FRET and FLIM. Molecules *17*, 4047-4132. 10.3390/molecules17044047.

29.	Reits, E.A., and Neefjes, J.J. (2001). From fixed to FRAP: measuring protein mobility and activity in living cells. Nat Cell Biol *3*, E145-147. 10.1038/35078615.

30.	Anzalone, A.V., Randolph, P.B., Davis, J.R., Sousa, A.A., Koblan, L.W., Levy, J.M., Chen, P.J., Wilson, C., Newby, G.A., Raguram, A., and Liu, D.R. (2019). Search-and-

replace genome editing without double-strand breaks or donor DNA. Nature *576*, 149-157. 10.1038/s41586-019-1711-4.

31. Wakabayashi, N., Itoh, K., Wakabayashi, J., Motohashi, H., Noda, S., Takahashi, S., Imakado, S., Kotsuji, T., Otsuka, F., Roop, D.R., et al. (2003). Keap1-null mutation leads to postnatal lethality due to constitutive Nrf2 activation. Nat Genet *35*, 238-245. 10.1038/ng1248.

32. Noda, N.N., and Fujioka, Y. (2015). Atg1 family kinases in autophagy initiation. Cell Mol Life Sci *72*, 3083-3096. 10.1007/s00018-015-1917-z.

33. Yamamoto, H., Fujioka, Y., Suzuki, S.W., Noshiro, D., Suzuki, H., Kondo-Kakuta, C., Kimura, Y., Hirano, H., Ando, T., Noda, N.N., and Ohsumi, Y. (2016). The Intrinsically Disordered Protein Atg13 Mediates Supramolecular Assembly of Autophagy Initiation Complexes. Dev Cell *38*, 86-99. 10.1016/j.devcel.2016.06.015.

34. Fujioka, Y., Alam, J.M., Noshiro, D., Mouri, K., Ando, T., Okada, Y., May, A.I., Knorr, R.L., Suzuki, K., Ohsumi, Y., and Noda, N.N. (2020). Phase separation organizes the site of autophagosome formation. Nature *578*, 301-305. 10.1038/s41586-020-1977-6.

35. Russell, R.C., Tian, Y., Yuan, H., Park, H.W., Chang, Y.Y., Kim, J., Kim, H., Neufeld, T.P., Dillin, A., and Guan, K.L. (2013). ULK1 induces autophagy by phosphorylating Beclin-1 and activating VPS34 lipid kinase. Nat Cell Biol *15*, 741-750. 10.1038/ncb2757.

36. Wold, M.S., Lim, J., Lachance, V., Deng, Z., and Yue, Z. (2016). ULK1-mediated phosphorylation of ATG14 promotes autophagy and is impaired in Huntington's disease models. Mol Neurodegener *11*, 76. 10.1186/s13024-016-0141-0.

37. Park, J.M., Jung, C.H., Seo, M., Otto, N.M., Grunwald, D., Kim, K.H., Moriarity, B., Kim, Y.M., Starker, C., Nho, R.S., et al. (2016). The ULK1 complex mediates MTORC1 signaling to the autophagy initiation machinery via binding and phosphorylating ATG14. Autophagy *12*, 547-564. 10.1080/15548627.2016.1140293.

38. Papinski, D., Schuschnig, M., Reiter, W., Wilhelm, L., Barnes, C.A., Maiolica, A., Hansmann, I., Pfaffenwimmer, T., Kijanska, M., Stoffel, I., et al. (2014). Early steps in autophagy depend on direct phosphorylation of Atg9 by the Atg1 kinase. Mol Cell *53*, 471-483. 10.1016/j.molcel.2013.12.011.

39. Joo, J.H., Wang, B., Frankel, E., Ge, L., Xu, L., Iyengar, R., Li-Harms, X., Wright, C., Shaw, T.I., Lindsten, T., et al. (2016). The Noncanonical Role of ULK/ATG1 in ER-to-Golgi Trafficking Is Essential for Cellular Homeostasis. Mol Cell *62*, 491-506. 10.1016/j.molcel.2016.04.020.

40. Li, T.Y., Sun, Y., Liang, Y., Liu, Q., Shi, Y., Zhang, C.S., Zhang, C., Song, L., Zhang, P., Zhang, X., et al. (2016). ULK1/2 Constitute a Bifurcate Node Controlling Glucose Metabolic Fluxes in Addition to Autophagy. Mol Cell *62*, 359-370. 10.1016/j.molcel.2016.04.009.

41. Konno, H., Konno, K., and Barber, G.N. (2013). Cyclic dinucleotides trigger ULK1 (ATG1) phosphorylation of STING to prevent sustained innate immune signaling. Cell *155*, 688-698. 10.1016/j.cell.2013.09.049.

42. Sanchez-Martin, P., Saito, T., and Komatsu, M. (2019). p62/SQSTM1: 'Jack of all trades' in health and cancer. FEBS J *286*, 8-23. 10.1111/febs.14712.

43. Sugase, K., Dyson, H.J., and Wright, P.E. (2007). Mechanism of coupled folding and binding of an intrinsically disordered protein. Nature *447*, 1021-1025. 10.1038/nature05858.

44. Wright, P.E., and Dyson, H.J. (2015). Intrinsically disordered proteins in cellular signalling and regulation. Nat Rev Mol Cell Biol *16*, 18-29. 10.1038/nrm3920.

45. Zhang, G., Wang, Z., Du, Z., and Zhang, H. (2018). mTOR Regulates Phase Separation of PGL Granules to Modulate Their Autophagic Degradation. Cell *174*, 1492-1506 e1422. 10.1016/j.cell.2018.08.006.

46. Yamasaki, A., Alam, J.M., Noshiro, D., Hirata, E., Fujioka, Y., Suzuki, K., Ohsumi, Y., and Noda, N.N. (2020). Liquidity Is a Critical Determinant for Selective Autophagy of Protein Condensates. Mol Cell *77*, 1163-1175 e1169. 10.1016/j.molcel.2019.12.026.

47. Itoh, K., Chiba, T., Takahashi, S., Ishii, T., Igarashi, K., Katoh, Y., Oyake, T., Hayashi, N., Satoh, K., Hatayama, I., et al. (1997). An Nrf2/small Maf heterodimer mediates the induction of phase II detoxifying enzyme genes through antioxidant response elements. Biochem Biophys Res Commun *236*, 313-322. 10.1006/bbrc.1997.6943.

48. Yanagawa, T., Itoh, K., Uwayama, J., Shibata, Y., Yamaguchi, A., Sano, T., Ishii, T., Yoshida, H., and Yamamoto, M. (2004). Nrf2 deficiency causes tooth decolourization due to iron transport disorder in enamel organ. Genes Cells *9*, 641-651. 10.1111/j.1356-9597.2004.00753.x.

49. Braun, S., Hanselmann, C., Gassmann, M.G., auf dem Keller, U., Born-Berclaz, C., Chan, K., Kan, Y.W., and Werner, S. (2002). Nrf2 transcription factor, a novel target of keratinocyte growth factor action which regulates gene expression and inflammation in the healing skin wound. Mol Cell Biol *22*, 5492-5505. 10.1128/MCB.22.15.5492-5505.2002.

50. Gurumurthy, C.B., Sato, M., Nakamura, A., Inui, M., Kawano, N., Islam, M.A., Ogiwara, S., Takabayashi, S., Matsuyama, M., Nakagawa, S., et al. (2019). Creation of CRISPR-based germline-genome-engineered mice without ex vivo handling of zygotes by i-GONAD. Nat Protoc *14*, 2452-2482. 10.1038/s41596-019-0187-x.

51. Yuza, K., Nakajima, M., Nagahashi, M., Tsuchida, J., Hirose, Y., Miura, K., Tajima, Y., Abe, M., Sakimura, K., Takabe, K., and Wakai, T. (2018). Different Roles of Sphingosine Kinase 1 and 2 in Pancreatic Cancer Progression. J Surg Res *232*, 186-194. 10.1016/j.jss.2018.06.019.

52. Mishina, M., and Sakimura, K. (2007). Conditional gene targeting on the pure C57BL/6 genetic background. Neurosci Res *58*, 105-112. 10.1016/j.neures.2007.01.004.

53. Uchihashi, T., Kodera, N., and Ando, T. (2012). Guide to video recording of structure dynamics and dynamic processes of proteins by high-speed atomic force microscopy. Nat Protoc *7*, 1193-1206. 10.1038/nprot.2012.047.

54. Ngo, K.X., Kodera, N., Katayama, E., Ando, T., and Uyeda, T.Q. (2015). Cofilin-induced unidirectional cooperative conformational changes in actin filaments revealed by high-speed atomic force microscopy. Elife *4*. 10.7554/eLife.04806.

55. Arai, R., and Waguri, S. (2019). Improved Electron Microscopy Fixation Methods for Tracking Autophagy-Associated Membranes in Cultured Mammalian Cells. Methods Mol Biol *1880*, 211-221. 10.1007/978-1-4939-8873-0_13.

56. Schindelin, J., Arganda-Carreras, I., Frise, E., Kaynig, V., Longair, M., Pietzsch, T., Preibisch, S., Rueden, C., Saalfeld, S., Schmid, B., et al. (2012). Fiji: an open-source platform for biological-image analysis. Nat Methods *9*, 676-682. 10.1038/nmeth.2019.

57. Amyot, R., and Flechsig, H. (2020). BioAFMviewer: An interactive interface for simulated AFM scanning of biomolecular structures and dynamics. PLoS Comput Biol *16*, e1008444. 10.1371/journal.pcbi.1008444.

Ikeda et al., Figure 1
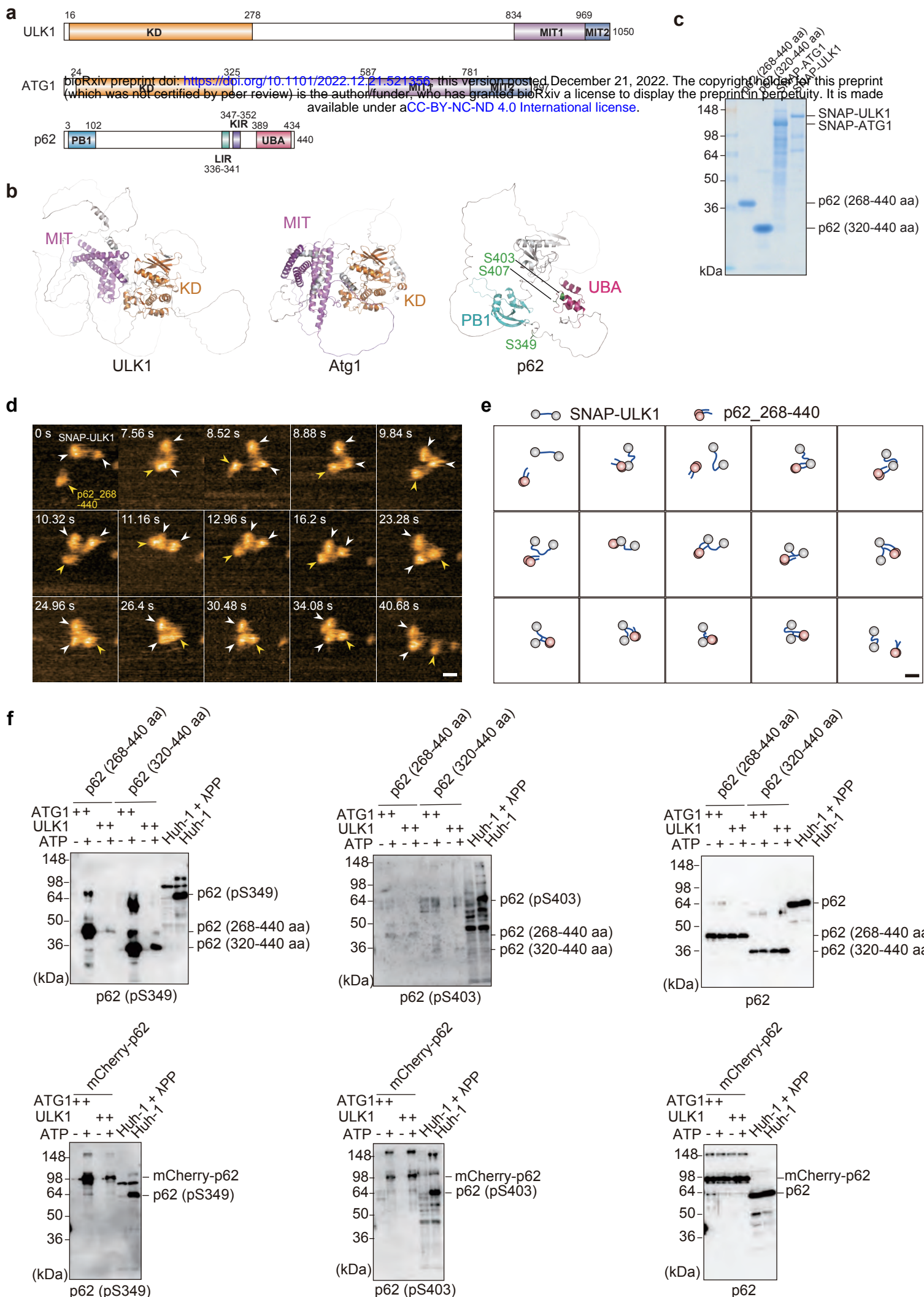
Ikeda et al., Figure 2
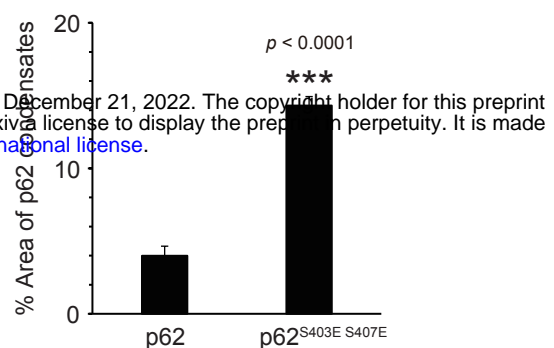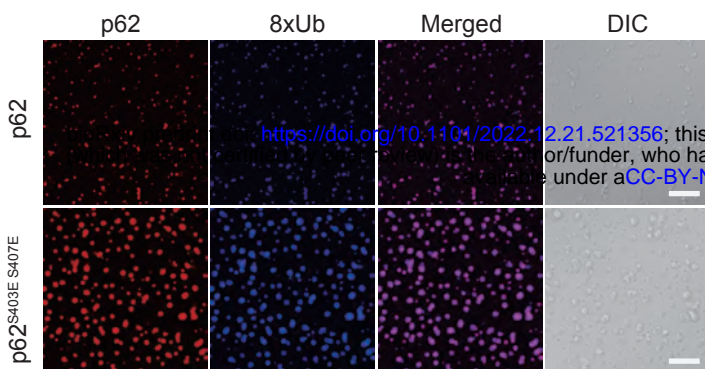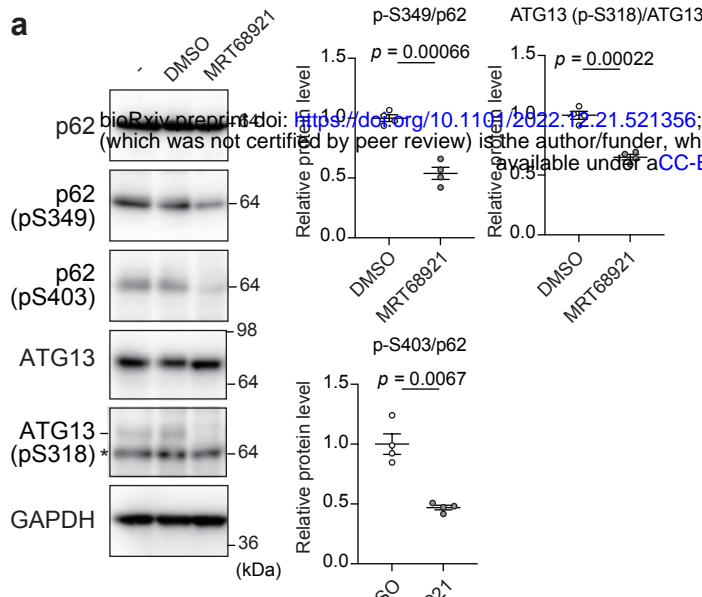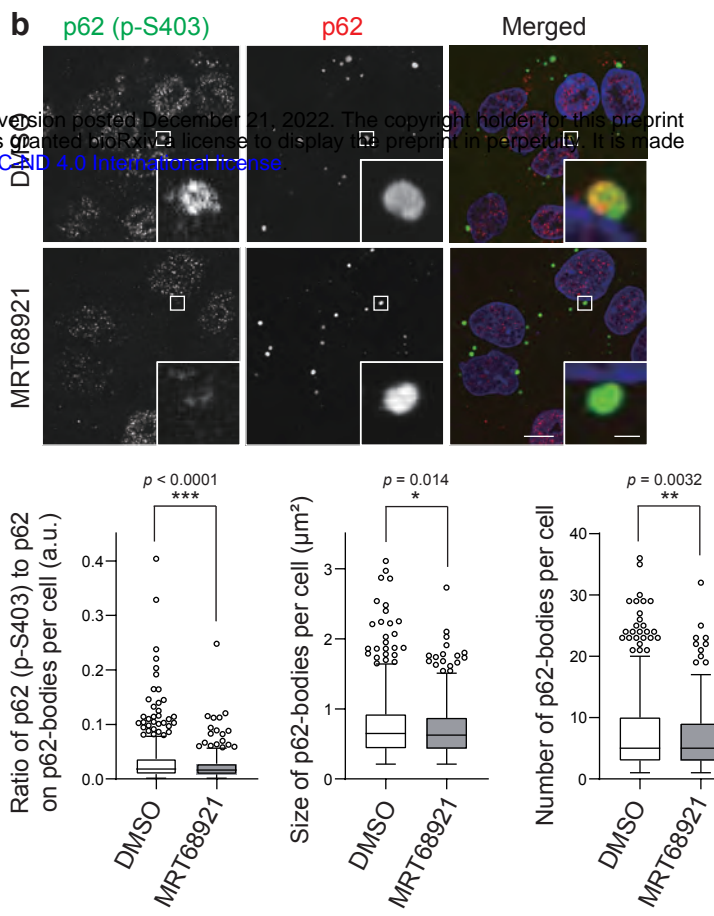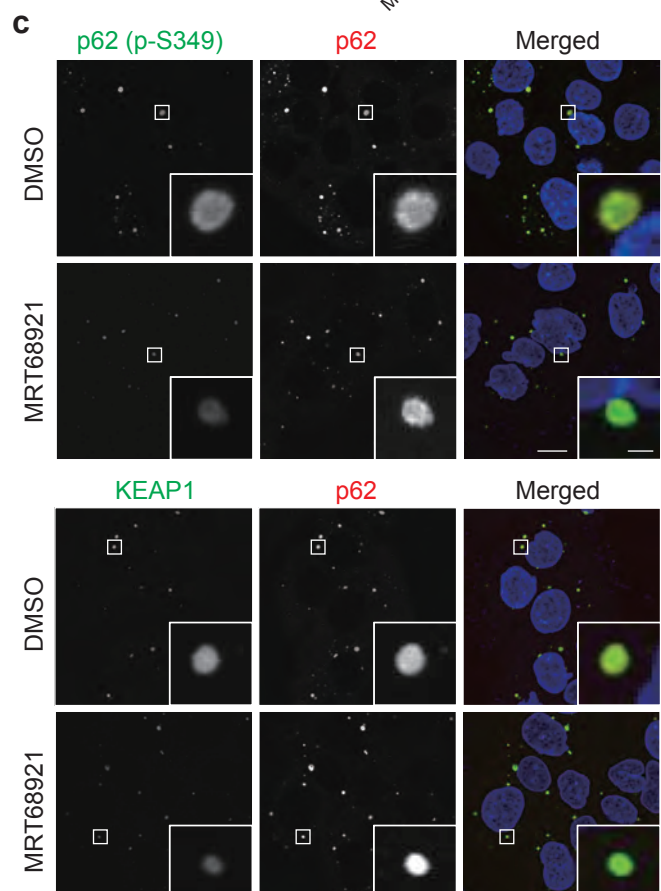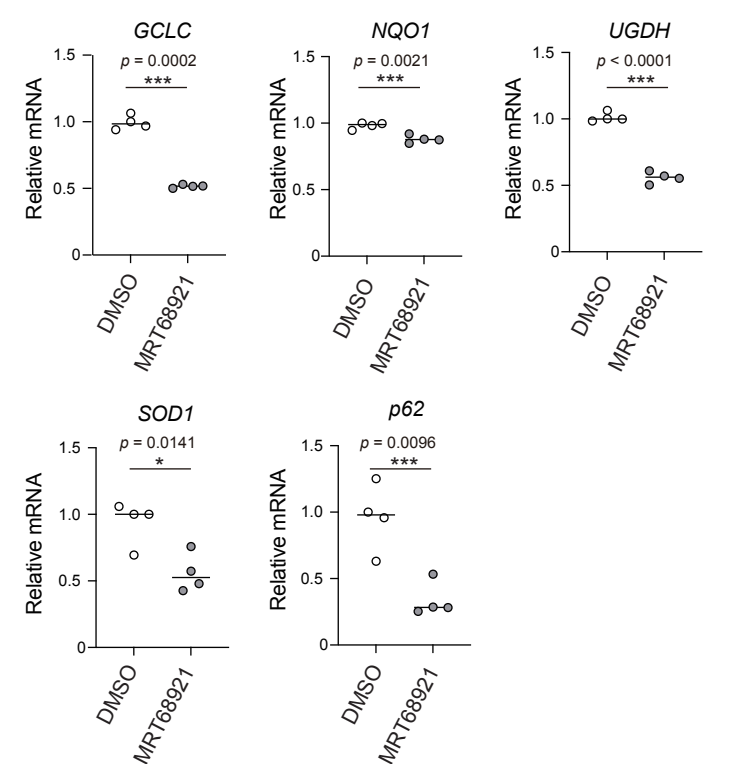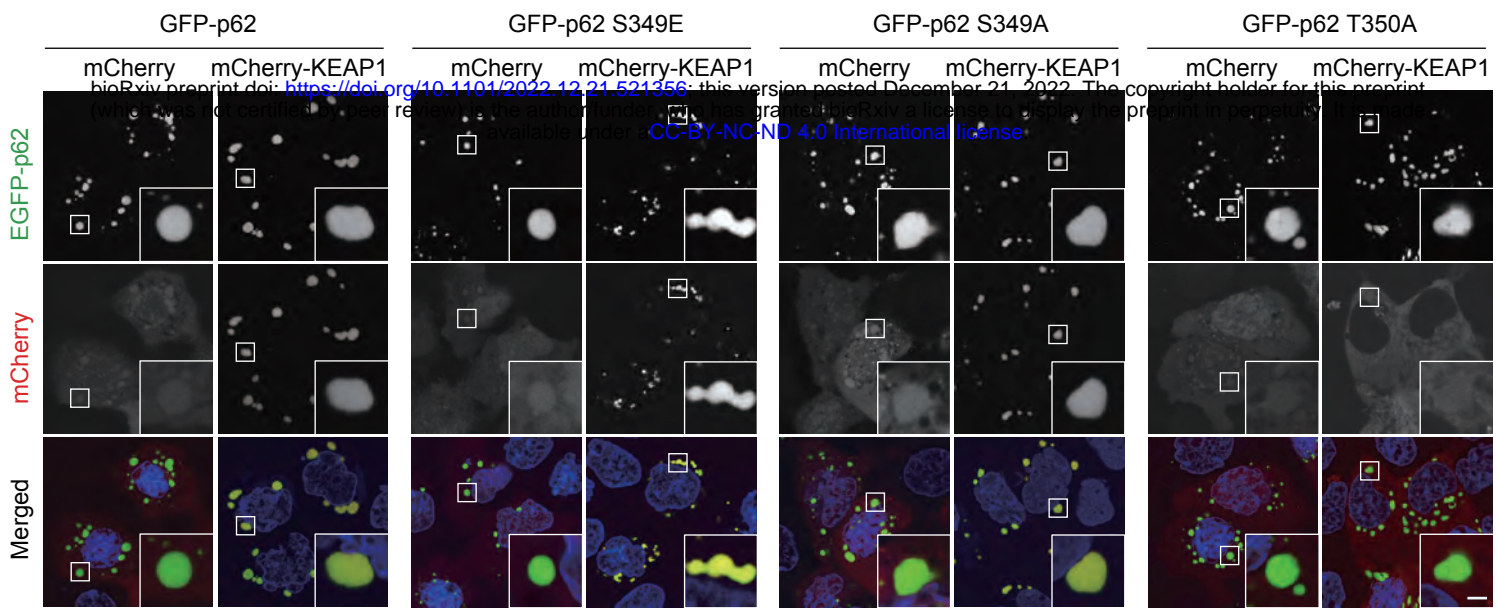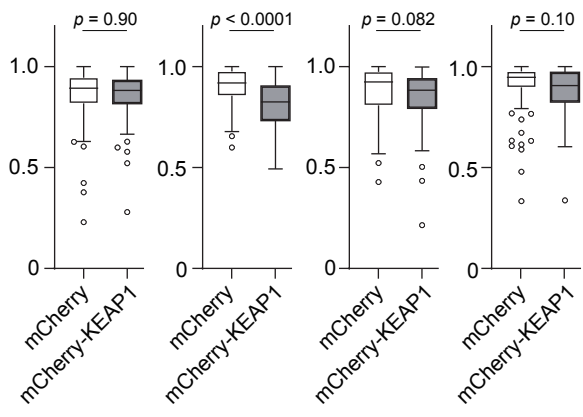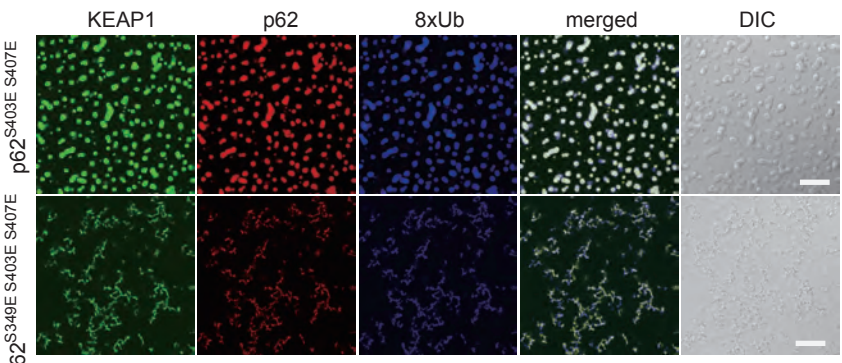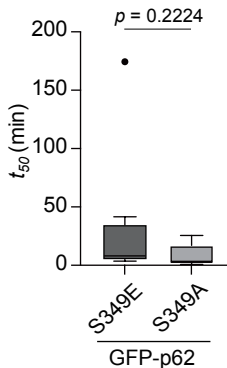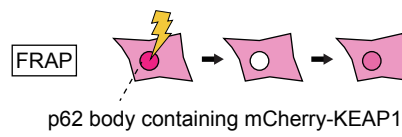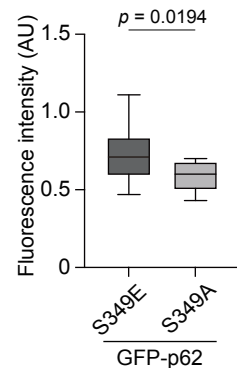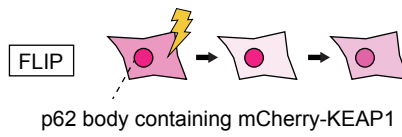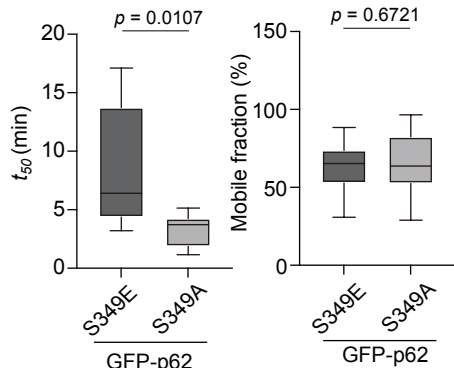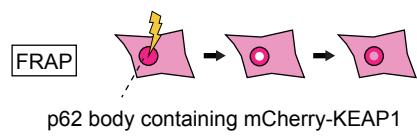
Ikeda et al., Figure 3

Ikeda et al., Figure 4

Ikeda et al., Figure 5